Diurnal, seasonal and long-term variations of global formaldehyde columns inferred from combined OMI and GOME-2 observations

I. De Smedt[1], T. Stavrakou[1], F. Hendrick[1], T. Danckaert[1], T. Vlemmix[1], G. Pinardi[1], N. Theys[1], C. Lerot[1], C. Gielen[1], C. Vigouroux[1], C. Hermans[1], C. Fayt[1], P. Veefkind[2], J.-F. Müller[1], and M. Van Roozendael[1].

[1] {Belgian Institute for Space Aeronomy (BIRA-IASB), Brussels, Belgium}

[2] {Royal Netherlands Meteorological Institute (KNMI), De Bilt, The Netherlands}

Correspondence to: Isabelle De Smedt (isabelle.desmedt@aeronomie.be)

1 **Abstract**

2 We present the new version (v14) of the BIRA-IASB algorithm for the retrieval of

3 formaldehyde (H$_2$CO) columns from spaceborne UV-Visible sensors. Applied to OMI

4 measurements from Aura and to GOME-2 measurements from MetOp-A and B, this

5 algorithm is used to produce global distributions of H$_2$CO representative of mid-morning and

6 early afternoon conditions. Its main features include (1) a new iterative DOAS scheme

7 involving three fitting intervals to better account for the O$_2$-O$_2$ absorption, (2) the use of

8 earthshine radiances averaged in the equatorial Pacific as reference spectra, (3) a destriping

9 correction and background normalisation resolved in the ~~along~~across-swath position. For the

10 air mass factor calculation, *a priori* vertical profiles calculated by the IMAGES chemistry

11 transport model at 09:30 am and 13:30 pm are used. Although the resulting GOME-2 and

12 OMI H$_2$CO vertical columns are found to be highly correlated, some systematic differences

13 are observed. Afternoon columns are generally larger than morning ones, especially in mid-

14 latitude regions. In contrast, over tropical rainforests, morning H$_2$CO columns significantly

15 exceed those observed in the afternoon. These differences are discussed in terms of the H$_2$CO

16 column variation between mid-morning and early afternoon, using ground-based MAX-

17 DOAS measurements available from seven stations in Europe, China and Africa. Validation

18 results confirm the capacity of the combined satellite measurements to resolve diurnal

19 variations in H$_2$CO columns. Furthermore, vertical profiles derived from MAX-DOAS

20 measurements in the Beijing area and in Bujumbura are used for a more detailed validation

21 exercise. In both regions, we find an agreement better than 15% when MAX-DOAS profiles

are used as *a priori* for the satellite retrievals. Finally regional trends in H_2CO columns are estimated for the 2004-2014 period using SCIAMACHY and GOME-2 data for morning conditions, and OMI for early afternoon conditions. Consistent features are observed such as an increase of the columns in India and Central-East China, and a decrease in Eastern US and Europe. We find that the higher horizontal resolution of OMI combined to a better sampling and a more favourable illumination at mid-day allow for more significant trend estimates, especially over Europe and North America. Importantly, in some parts of the Amazonian forest, we observe with both time series a significant downward trend in H_2CO columns, spatially correlated with areas affected by deforestation.

1 Introduction

Atmospheric formaldehyde (H_2CO) is an intermediate product common to the degradation of many volatile organic compounds. While the global formaldehyde background is due to methane oxidation, emissions of non-methane volatile organic compounds (NMVOCs) from biogenic, biomass burning and anthropogenic continental sources result in important and localised production of H_2CO. The global sink of H_2CO is due to photolysis and oxidation by OH, resulting in a photochemical lifetime of only a few hours. Elevated concentrations of H_2CO can therefore be related to the emission of reactive NMVOCs. Monitoring the spatial and temporal variability of NMVOC emissions is essential for a better understanding of the processes that not only control the production and the evolution of tropospheric ozone, key actor in air quality and climate change, but also of the hydroxyl radical OH and secondary organic aerosols. For these reasons, H_2CO satellite observations have been increasingly used in combination with tropospheric chemistry transport models to constrain NMVOC emissions ~~in top-down inversion approaches~~ (*i.a.* Palmer et al., 2006; Fu et al., 2007; Millet et al., 2008; Stavrakou et al., 2009a, 2009b; 2014; Curci et al., 2010; Barkley et al., 2013: Fortems-Cheiney et al., 2012; Marais et al., 2012, Zhu et al., 2014).

For more than 15 years, mid-morning formaldehyde tropospheric columns have been retrieved from the successive nadir scanning spectrometers GOME on ERS-2 (1996-2003) (Chance et al., 2000; Palmer et al., 2001; De Smedt et al., 2008), SCIAMACHY on ENVISAT (2002-2011) (Wittrock et al., 2006; De Smedt et al., 2008) and GOME-2 on MetOp-A & B (2006- & 2012-) (De Smedt et al., 2012; Hewson et al., 2013). Since 2004, complementary early afternoon H_2CO columns can also be retrieved from the imaging spectrometer OMI on Aura (Kurosu, 2008; Millet et al., 2008; González Abad et al., 2015a),

and since 2011 from OMPS on SUOMI-NPP (Li et al., 2015; González Abad et al., 2015b). In addition to formaldehyde, glyoxal – another short-lived NMVOC – has also successfully been retrieved from SCIAMACHY (Wittrock et al., 2006), GOME-2 (Vrekoussis et al., 2010; Lerot et al., 2010) and OMI (Alvarado et al., 2014; Chan Miller et al., 2014).

From 2017 onward, the morning observations will be continued with a third GOME-2 instrument to be launched on MetOp-C (Callies et al., 2000), while the afternoon observations will be extended with the TROPOMI instrument (Veefkind et al., 2012), to be launched in 2016 as part of the Copernicus Sentinel 5 Precursor (S-5P) mission, and later with the Sentinel-5 mission to be operated on the MetOp Second Generation platform (Ingmann et al., 2012). Also at the 2020 horizon, the Sentinel-4 instrument on the geostationary Meteosat Third Generation (MTG) platform will allow for hourly observations of H_2CO over Europe, while TEMPO (NASA) and GEMS (KARI) will provide geostationary measurements for North America and Asia respectively. To realize the full potential of these missions, it is crucial to develop high quality and consistent retrieval algorithms applicable to the different satellite sensors, taking into account their differences in horizontal resolution and sampling. Likewise, it is essential to understand the diurnal variations of the sources and sinks of formaldehyde, in order to exploit the synergy between the morning and afternoon satellite observations. To our knowledge, so far, the use of combined morning and afternoon H_2CO satellite observations has only been reported over Amazonia, using SCIAMACHY and OMI measurements (Barkley et al., 2011; 2013).

Ground-based measurements are essential to quantitatively assess the seasonal and diurnal variations of the tropospheric H_2CO columns. However, up to now, very few validation studies have been reported for satellite H_2CO observations (Wittrock et al., 2006; Vigouroux et al., 2009) because of the general lack of suitable ground-based measurements, in particular for tropical regions where H_2CO columns are among the highest worldwide (Stavrakou et al., 2009b; Marais et al., 2012; Barkley et al., 2013). Also, very little attention has been paid to the diurnal variations of the H_2CO columns and to their local dependencies, which are a complex blend of local NMVOC emission variations, H_2CO production and loss via oxidation and photolysis depending on local chemical regimes and season. To this regard, the latest generation of MAX-DOAS instruments and retrieval algorithms offer new perspectives for the validation of tropospheric trace gas concentrations and aerosol optical densities (Clémer et al., 2010; Pinardi et al., 2013; Vlemmix et al., 2014; Wang et al., 2014).

This study focuses on tropospheric formaldehyde retrievals from OMI, using an algorithm historically developed within the TEMIS (Tropospheric Emission Monitoring Internet Service) framework and applied to morning observations from the GOME, SCIAMACHY and GOME-2 sensors (http://h2co.aeronomy.be). We present several adaptations that have been implemented to handle observations from the OMI imaging spectrometer, as well as number of more general improvements to the algorithm, giving rise to a new version of the BIRA-IASB H_2CO retrieval algorithm (version 14). This version has been applied to the complete time series of OMI measurements, as well as to the GOME-2 measurements from MetOp-A and B platforms. For the first time, differences between morning and afternoon H_2CO columns are estimated at the global scale and discussed in terms of H_2CO diurnal variations, horizontal resolution effects and retrieval uncertainties. Moreover, ground-based measurements at seven stations, covering mid-latitude and tropical locations, are used to validate the observed H_2CO columns and their diurnal changes as derived from the combined satellite data sets.

The paper is structured as follows: section 2 introduces the main characteristics of the OMI and GOME-2 instruments. Section 3 describes the new version (v14) of the H_2CO retrieval algorithm. The H_2CO tropospheric columns obtained from GOME-2 and OMI measurements are presented and compared in section 4, and the main results of our validation studies are outlined in section 5. Finally, the long-term variations of the H_2CO columns over the last decade are discussed in section 6.

2   Satellite instruments

2.1   OMI on Aura

The Aura satellite was launched in July 2004, in a sun-synchronous polar orbit crossing the equator around at 13:30 LT (in ascending mode). It is the third major component of the NASA Earth Observing System (EOS) following Terra (launched 1999) and Aqua (launched 2002). OMI (Ozone Monitoring Instrument) is a nadir viewing imaging spectrometer that measures the solar radiation backscattered by the Earth's atmosphere and surface over the wavelength range from 270 to 500 nm with a spectral resolution of about 0.5 nm (Levelt et al., 2006). The light entering the telescope is depolarised using a scrambler and then split into two channels: a UV channel (wavelength range 270 - 380 nm) and a VIS channel (wavelength range 350 - 500 nm). The 114° viewing angle of the telescope corresponds to a 2600 km wide swath on the earth surface, which enables nearly daily global coverage. In the nominal global operation

mode, the OMI ground pixel size varies from 13x24 km² at nadir to 28x150 km² at the edges of the swath. For this work, we have used the OMI Level 1B UV Global Radiances Data Product (OML1BRUG - Version 003) provided on the NASA website (http://disc.sci.gsfc.nasa.gov/Aura/data-holdings/OMI/oml1brug_v003.shtml).

2.2 GOME-2 on MetOp-A & B

The MetOp-A and MetOp-B satellites were respectively launched in October 2006 and September 2012, in sun-synchronous polar orbits with equator crossing times of 09:30 and 09:00 LT (in descending node). Both satellites carry the same type of GOME-2 (Global Ozone Monitoring Experiment) instruments. Hereinafter, we will refer to them by GOME-2A and GOME-2B (or G2A and G2B). GOME-2 (Callies et al., 2000; Munro et al., 2006) is an improved version of the GOME instrument which flew on the ERS-2 satellite. It is a nadir viewing scanning spectrometer with four main optical channels, covering the spectral range between 240 and 790 nm with a spectral resolution between 0.26 nm and 0.51 nm. Additionally, two polarisation components are measured with polarisation measurements devices (PMDs) at 30 broad-band channels covering the full spectral range. A direct sun spectrum is also measured via a diffuser plate once per day. The default swath width of the GOME-2 scan is 1920 km allowing for global Earth coverage within 1.5–3 days at the equator. The nominal ground pixel size is 80×40 km^2. For this work, we have used the EUMETSAT GOME-2A and GOME-2B level 1B data version 5.3.0 from the beginning of their time series up to mid-June 2014, and version 6.0.0 afterwards.

3 Formaldehyde retrievals

We use a DOAS algorithm (Differential Optical Absorption Spectroscopy), including three main steps, further detailed in Sect. 3.1, 3.2 and 3.3: (1) the fit of absorption cross-section databases to the log-ratio of measured Earth reflectance to retrieve H$_2$CO slant columns (N_s), (2) a background normalisation procedure to eliminate remaining unphysical dependencies, and (3) the calculation of tropospheric air mass (M) factors using radiative transfer calculations and modelled *a priori* profiles. The tropospheric H$_2$CO vertical column (N_v) is related to intermediate quantities by the equation:

$$N_v = \frac{\Delta N_s}{M} + N_{v,0,CTM}$$

where ΔN_s is the background-corrected slant column density, and $N_{v,0,CTM}$ is the model background column in the reference sector. More detailed equations can be found in our previous publications (e.g. De Smedt et al., 2011 and 2014).

~~Since 10 years, the TEMIS website provides l~~Level 2 formaldehyde products developed at BIRA-IASB are provided via the TEMIS website~~, for all European nadir viewing UV-VIS spectrometers~~. The algorithms used to generate these products ~~were~~ are designed to be as consistent as possible, in order to optimise the overall coherency of the resulting time series. Over the years, scientific developments are leading to step-by-step improvements in the quality of the data products. This entails regular reprocessing of the datasets. The retrieval settings presented here for the GOME-2 and OMI measurements are based on the BIRA algorithm developed for GOME-2 (De Smedt et al., 2012) but include a number of adaptations allowing for the efficient processing of imaging instruments, and additional improvements as further detailed in this section. The main differences compared to version 12 are (1) the use of daily radiances as DOAS reference spectra, (2) the inclusion of O_2-O_2 in the BrO and H_2CO retrieval intervals and (3) the pre-fit of O_2-O_2 in a dedicated retrieval interval. For the reference sector correction, which so far was resolved in latitude and time, an additional dimension (viewing zenith angle or detector row) is now introduced as destriping procedure. An updated version of the IMAGES model *a priori* profiles is sampled~~used~~ at the respective satellite overpass times. Quality flags have been defined, in order to better select the valid satellite observations. Finally, the format of the level 2 data files has been changed to HDF-5. As for the previous algorithm versions, level 2 and level 3 data products of version 14 are openly available on TEMIS (http://h2co.aeronomie.be). Comparisons between the BIRA-IASB OMI H_2CO product and the OMI operational product from SAO can be found in González Abad et al. (2015b), while comparisons with the NASA OMPS PCA product can be found in Li et al. (2015).

3.1 Slant Columns

The formaldehyde slant columns are retrieved in the interval 328.5-346 nm. Retrieval settings are summarized in Table 1~~Table 1~~. We use the QDOAS software developed at BIRA-IASB for the DOAS retrieval of trace gases from many common satellite and ground-based instruments. QDOAS is distributed under the GNU GPL license version 2.0 (Danckaert, Fayt and Van Roozendael, 2014, http://uv-vis.aeronomie.be/software/QDOAS).

In QDOAS, the wavelength registration of the reference spectrum is fine-tuned by means of a calibration procedure making use of the solar Fraunhofer lines. To this end, a highly accurate reference solar atlas (Chance and Kurucz, 2010) is degraded at the resolution of the instrument, through convolution by the instrumental slit function. The absorption cross sections of the different trace gases are also convolved with the instrumental slit function. In the case of GOME-2, the slit function shape is fitted during the calibration procedure, in order to take into account its changes with time (Dikty and Richter, 2011; De Smedt et al., 2012). In the case of OMI, pre-flight measured slit functions (Dobber et al., 2006) are used, and the calibration is performed for each binned spectrum of the detector array (60 rows). Except for the reported row anomaly that has dynamically evolved over the years (http://www.knmi.nl/omi/research/product/rowanomaly-background.php), the performance of the OMI instrument has proven to be very stable in time (Dobber et al., 2008). In contrast to previous work, we now moved to the systematic use of daily radiance spectra averaged in the equatorial Pacific (15°S-15°N, 180°E-240°E) as reference for the DOAS retrieval. Different reference spectra are selected daily for each OMI row and their wavelength registration is optimised as described above. This serves as a first correction for the OMI stripe effect. Consequently, all retrieved slant columns are differential columns relative to the mean reference spectra.

A 5th order polynomial is used to fit the low-frequency variations of the spectra, as well as a linear offset term. The H_2CO Meller and Moortgat (2000) laboratory measurements are fitted to the differential absorption features. The absorption cross-sections of O_3 at 228K and 243K, NO_2 and BrO are included. To take into account the Ring effect, two cross-sections are used (Vountas et al., 1998). They have been calculated in an ozone-containing atmosphere for low and high SZA using LIDORT RRS (Spurr et al., 2008). Two additional terms (called O_3L and O_3O_3 in Table 1Table 1), resulting from the Taylor expansion of the O_3 absorption as a function of the wavelength, are included in order to better cope with strong O_3 absorption effects (Puķīte et al; 2010; De Smedt et al., 2012). Introduced in the previous version 12, a second (larger) retrieval interval is used to pre-fit the BrO slant columns (Fig.1). The benefit of this procedure is to decorrelate the H_2CO and BrO absorption features, resulting in a reduction of the noise on the BrO and H_2CO slant columns. However the O_2-O_2 (O_4) absorption had not been taken into account in version 12, neither in the larger nor in the shorter interval. While the weak and smooth O_4 signature appears to be well fitted by the 5th order polynomial used in the shorter interval (Hewson et al., 2013), not including the stronger

O$_4$ term in the larger interval is clearly a shortcoming. Nevertheless, this solution has often been selected in past studies, because experience has shown that including O$_4$ tends to destabilize the BrO fit (Kurosu, 2008; Begoin et al., 2010; Theys et al., 2011) hence leading to increased noise on the H$_2$CO slant columns retrieved in the shorter interval. In version 14, we propose the addition of a third fitting interval (339-364 nm) covering the entire O$_4$ absorption band around 360 nm (Fig.1). We use the recently published O$_4$ absorption cross-sections by Thalman and Volkamer (2013), and our H$_2$CO retrieval scheme therefore now includes three fitting intervals: w1 for the pre-fit of O$_4$, w2 for the pre-fit of BrO, and w3 for the fit of the H$_2$CO slant columns, in which the O$_4$ and BrO slant columns are fixed to values determined in the other intervals.

It should be noted that for the GOME and SCIAMACHY H$_2$CO retrievals, only one retrieval interval is used (328.5-346 nm) because the quality of the recorded spectra has been found to be insufficient in the 360 nm region (De Smedt et al., 2008). O$_4$ absorption effects are therefore significantly reduced.

Table 1 : Summary of retrieval settings used in version 14 of the BIRA H$_2$CO retrieval algorithm, applicable to GOME-2 and OMI measurements.

Settings for the DOAS equation parameters		
Calibration	Accurate solar atlas (Chance and Kurucz, 2010)	
Slit function	OMI: 1 slit function per binned spectrum as a function of wavelength (Dobber et al., 2006)	GOME-2: asymmetric Gaussian slit function fitted during calibration (De Smedt et al., 2012)
Reference spectrum	Daily average of radiances selected in the equatorial Pacific	
Polynomial	5th order	
Intensity offset	Linear offset	
Hot pixels treatment	Iterative spike removal algorithm (Richter et al., 2011, De Smedt et al., 2014)	
Absorption cross-section datasets		
H$_2$CO	Meller and Moortgat (2000)	
O$_3$	Brion et al. (1998); Daumont et al. (1992); Malicet et al. (1995)	
BrO	Fleischmann et al. (2004)	
NO$_2$	Vandaele et al. (2002)	
O$_2$-O$_2$ (O$_4$)	Thalman and Volkamer (2013)	
Ring effect	2 Ring cross-sections calculated in an ozone containing atmosphere for low and high SZA, using LIDORT RRS (Spurr et al., 2008).	
Non-linear O$_3$ absorption effect	2 pseudo-cross sections from the Taylor expansion of the wavelength and the O$_3$ optical depth (Puķīte et al., 2010).	
Fitting interval w1: O$_4$	**339-364 nm**	
Included cross-sections	O$_4$ (293K), O$_3$ (228K), BrO (223K), H$_2$CO (298K), NO$_2$ (220K), Ring1, Ring2	
Fitting interval w2: BrO	**328.5-359 nm**	

Included cross-sections	BrO (223K), H_2CO (298K), O_3 (228K and 243K), NO_2 (220K), O_4 (293K, not fitted), Ring1, Ring2, O_3L, O_3O_3
Fitting interval w3: H_2CO	**328.5-346 nm**
Included cross-sections	H_2CO (298K), O_3 (228K and 243K), BrO (223K, not fitted), NO_2 (220K), O_4 (293K, not fitted), Ring1, Ring2, O_3L, O_3O_3

1 Figure 2 illustrates the correlation effects occurring between the O_4, BrO and H_2CO

2 absorptions, for one OMI orbit on July, 1st 2005. The upper panel shows the O_4 differential

3 slant columns retrieved in w1 (339-364 nm, light blue) or in w2 (328.5-359 nm, dark green)

4 as a function of the latitude. The improved quality of the O_4 slant columns in w1 is observed,

5 as expected from Fig.1. The second and third panels show the differences observed in the BrO

6 and H_2CO slant columns depending on whether O_4 is included in the fits or not (v14-v12), as

7 a function of the O_4 slant columns. Those differences are shown for two cases: O_4 slant

8 columns from w1 (light blue, v14) or from w2 (dark green). The pre-fit of O_4 in w1 does

9 reduce the noise on the O_4, BrO and H_2CO slant columns, in the three intervals. The

10 correlation between the 3 molecules is not reduced by the introduction of this third interval

11 (the slope of the differences remains the same), but the slant columns are limited to more

12 realistic values for each molecule, allowing for an effective reduction of the noise. It is

13 interesting to note that the observed slopes of the differences in BrO and H_2CO columns are

14 exactly the same for GOME-2 and OMI retrievals and for different periods of the years (not

15 shown), pointing to a fundamental spectral effect rather than an instrumental feature.

16 From Fig.2, one can conclude that the net effect of including O_4 in the fits is a positive

17 correlation of the H_2CO slant columns with the O_4 differential columns, with H_2CO column

18 deviations of less than 10^{16} molec.cm^{-2} but sometimes reaching 2×10^{16} molec.cm^{-2} for

19 extreme O_4 values. Figure 3 presents O_4 differential slant columns retrieved in w1 from OMI

20 measurements in February and August 2007, giving an idea of the spatial distribution of the

21 expected differences.

22 Over the Pacific Ocean, the O_4 differential slant columns are generally positive and increase

23 with the solar zenith angle. Figure 4 presents the averaged zonal variation of the H_2CO, BrO

24 and O_4 differential slant columns for January, April, July and October 2007, as a function of

25 the latitude (a) when O_4 is not included in the fit (v12), and (b) when O_4 is pre-fitted in w1

26 and included in the fit (v14). Dashed lines show the slant columns before the background

27 normalisation procedure. The decrease of the H_2CO slant columns with latitude is greatly

28 reduced when O_4 is considered, with a minimum impact on the standard deviations of the

29 columns, owing to the pre-fit of O_4. However, a positive artificial dependency remains, that is

related to ozone absorption interferences and still needs to be corrected (see Sect. 3.2). The O_4 effect is exactly the opposite for BrO, for which a decrease of the columns is observed for large O_4 slant columns (about -20%). This can have a significant impact for BrO studies in polar regions (Salawitch et al., 2010; Choi et al., 2012), but it is beyond the scope of this paper.

Over the continents, where H_2CO column enhancements are expected, the differential O_4 slant columns are almost always negative (*i.e.* lower than over oceans), due to the combined effect of higher altitude and lower surface reflectivity. We observe therefore a decrease of the H_2CO columns over continental emission regions, by 0 down to -25%. This reduction is the same for GOME-2 and OMI, i.e. it has no impact on the observed diurnal variations. As an example, Fig.5 presents the time series of GOME-2 and OMI H_2CO columns over India and Equatorial Africa, representative for mid-latitudes and tropical emission regions. Results without (v12) and with (v14) O_4 included are plotted, as well as the differences between OMI and GOME-2 for the 2 versions. A reduction of the columns is observed when including O_4 in the fits, but the OMI-GOME-2 differences are equivalent for v12 and v14.

3.2 Across-track and zonal reference sector correction

The use of daily radiance spectra as reference for the DOAS retrievals result in differential slant columns, close to zero in the equatorial Pacific. However, ~~Residual~~ latitude-dependent biases in the H_2CO columns, due to unresolved spectral interferences, remain a limiting factor for the DOAS retrieval of weak absorbers such as H_2CO. Furthermore, in the case of a 2D-detector array such as OMI, across-track striping arises, due to imperfect calibration and different dead/hot pixel masks for the detectors. Such instrumental effects also affect scanning spectrometers like GOME-2, but since these instruments have one single detector, these errors do not appear as stripes, but rather as constant offsets (Boersma et al., 2011). These different retrieval artefacts can be compensated to a certain extent, using normalisation approaches such as the reference sector correction (Kurosu, 2008; De Smedt et al., ~~2012~~2008). As for the DOAS reference radiance selection, the reference sector is chosen in the Pacific Ocean, where the only significant source of H_2CO is the CH_4 oxidation. The H_2CO background is replaced by model simulations in the same region. The reference sector correction is also meant to handle possible time-dependent instrumental degradation effects, for example the evolution of the OMI stripe artefacts, or the GOME-2 signal degradation (De Smedt et al., 2012). Note that our analysis show that the most efficient method to reduce across-track stripes in OMI H_2CO

retrievals is to use row-dependent mean radiances as reference spectrum in the DOAS equation (see Sect. 3.1).

We apply a 2-step normalisation of the H_2CO slant columns. In a first step, a row-dependent median H_2CO value is determined in the equatorial Pacific (15°S-15°N, 180°E-240°E) and subtracted from all the columns (in the case of GOME-2, we use a viewing angle-dependent correction). The aim is to reduce possible remaining offsets between rows, resulting from the different detectors. In addition to the destriping procedure, those OMI rows presenting a level of noise and fitting residuals significantly higher than the average of the other rows for a particular day, are assigned a bad quality flag, and not further used in our applications. This criterion removes a few rows from the analysis in 2005, and more importantly, all the rows affected by the row anomaly which started in June 2007, and further developed over the years (http://www.knmi.nl/omi/research/product/rowanomaly-background.php). As illustrated by the first line of Fig.6, the affected rows can be identified using the fitting residuals. This filtering procedure is less systematic than the use of flags provided in the level 1 files, and is aimed to keep as many observations as possible in the analysis, which is of fundamental importance to mitigate the noise on formaldehyde observations. In a second step, the latitudinal dependency of the offset-corrected H_2CO slant columns is modelled by a polynomial in the entire reference sector (90°S-90°N, 180°E-240°E). These two corrections are sequentially subtracted from the global slant columns and replaced by the latitudinal dependency of the modelled columns in the same region. The result of the across-track and zonal reference sector correction is illustrated in Fig.4 as a function of the latitude and in the second line of Fig.6, showing daily maps of normalised OMI H_2CO slant columns in 2005 and 2014. The loss of coverage due to the OMI row anomaly and to our filtering scheme is clearly visible when comparing the 2005 and 2014 maps.

3.3 Air Mass Factors

In the troposphere, scattering by air molecules, clouds and aerosols lead to complex altitude-dependent air mass factors. Multiple scattering calculations are required for the determination of the air mass factors, and the vertical distribution of the absorber has to be assumed *a priori*. In the case of optically thin absorbers, the formulation of Palmer et al. (2001) is used and has been described for the TEMIS H_2CO retrievals in De Smedt et al. (2012). It decouples the vertical sensitivity of the measurements (the scattering weighting functions, derived with radiative transfer model calculations) from the vertical profile shape of the species of interest

1   (vertical shape factors, taken from an atmospheric chemistry transport model or from some

2   other prior knowledge of the vertical distribution of the absorber). Details on these two

3   calculation steps are given below. The decoupling of the AMF calculation allows addressing

4   separately the radiative transfer effects, including clouds, and the atmospheric composition of

5   optically thin absorbers like H_2CO. Vertical columns might be improved for particular

6   locations by using more accurate *a priori* profiles, for example based on input from regional

7   models, ground-based or aircraft measurements. Furthermore, using shape factors from an

8   atmospheric chemistry model ensures consistency for subsequent evaluation of the model

9   with the retrieved vertical columns (Barkley et al., 2013). For these reasons, the averaging

10   kernels and the *a priori* profiles are provided in the level 2 data files for each individual

11   measurement. The third line of Fig.6 presents global daily maps of AMF in April 2005 and

12   2014. These maps have been filtered for effective cloud fractions larger than 0.4. Clouds and

13   *a priori* profile shapes are further discussed below and in the validation Section (5.2).

14   ### 3.3.1 Scattering weighting functions

15   Scattering weighting functions calculated at 340 nm, using the LIDORT v3.3 radiative

16   transfer model (Spurr, 2008) are tabulated according to their dependencies with solar, viewing

17   and relative azimuth angles, surface altitude and surface reflectivity. We use the surface

18   reflectivity data base derived from OMI by Kleipool et al. (2008), in both GOME-2 and OMI

19   H_2CO retrievals. Radiative cloud effects are corrected using the independent pixel

20   approximation (IPA, Martin et al., 2002) and the respective cloud products of the instruments

21   provided on the TEMIS website, namely the GOME-2 O_2 A-band Frescov6 product (Wang et

22   al., 2008) and the OMI O_4 cloud product (Stammes et al., 2008). While the cloud fractions are

23   in general good agreement between OMI and GOME-2, we observe larger discrepancies for

24   the cloud altitudes. ~~While t~~The differences between OMI and GOME-2 cloud-free AMFs

25   range from 0 to -10% (observation geometry effects), but the differences between IPA cloud-

26   corrected AMFs can reach -20% where and when the cloud lies in the lower troposphere. This

27   implies an uncertainty of about 10% in the final product, since it is not clear whether those

28   cloud-related differences reflect real differences in cloud properties or differences in the cloud

29   retrieval ~~–~~algorithms. This stresses the need for a multi-instrument homogenised cloud

30   product, for example based on the O_4 absorption band that can be measured by all sensors. No

31   explicit correction is applied for aerosols but the cloud correction scheme accounts for a large

32   part of their scattering effect (Boersma et al., 2011). The uncertainty related to aerosol effects

is estimated to be lower than 15% in average (Leitao et al., 2008; Castellanos et al., 2015; Theys et al., 2015).

3.3.2 Vertical shape factors: IMAGES-v2

The *a priori* profile shapes are extracted from daily simulations performed with the IMAGES model, at 09:30 am for GOME-2 and 13:30 pm for OMI. The IMAGESv2 CTM calculates the global distributions of 90 long-lived and 41 short-lived trace gases at a resolution of 2° (latitude) x 2.5° (longitude) and on 40 vertical levels from the surface to the lower stratosphere. The current model version is thoroughly described in Stavrakou et al. (2013). The model time step is set to 4 hours. Diurnal changes in the photolysis and kinetic rates, meteorological fields, and the emissions are taken into account through correction factors calculated from a simulation with a 20-min time step (Stavrakou et al., 2009a) and applied to model runs using longer time steps. Simulations have been performed for all years between 2005 and 2013, spun up by a period of four months.

Anthropogenic VOC emissions are obtained from the RETRO 2000 global database (Schultz et al., 2008) and are kept constant throughout the years. Over Asia, RETRO is overwritten by the REASv2 inventory (Kurokawa et al., 2013) until 2008, whereas 2008 values are used for more recent years. Anthropogenic VOC emissions are equal to 147 and 150 Tg VOC in 2005 and 2006, respectively, and to 156 Tg VOC for the following years. Emissions of isoprene from vegetation are taken from the MEGAN-MOHYCAN-v2 inventory (Stavrakou et al., 2014). The global annual fluxes range between 323 Tg and 363 Tg isoprene, the lowest and the highest values corresponding to 2008 and to 2010, respectively. Open biomass burning emissions are taken from the GFEDv3 inventory (van der Werf et al., 2010) until 2011, whereas a climatological mean based on 1997-2011 GFEDv3 emissions is used for 2012 and 2013. Global annual fire emissions range between 70 Tg VOC (in 2009) and 105 Tg VOC (in 2010).

The photochemical production of H_2CO is estimated at ca. 1600 Tg annually. The main formaldehyde sinks are the oxidation by OH (Sander et al., 2011) which leads to CO production and conversion of OH to HO_2, and two photolysis reactions which produce CO and HO_2 radicals. Based on IMAGESv2 model calculations, photolysis is by far the dominant removal process, estimated at 71% of the global sink, whereas the OH sink is less efficient (26%). Photolysis of H_2CO and oxidation by OH account for about 71% and 26% of the

1 ~~global sink, respectively, while d~~Dry and wet deposition account for the remainder (<3%).

2 The global photochemical H_2CO lifetime is estimated at 4.5 hours.

3.4 Quality criteria of the H_2CO vertical columns

4 The H_2CO level-2 files of version 14 are provided in HDF-5 format. They include all the

5 intermediate quantities of the H_2CO retrieval from slant columns to vertical columns, air mass

6 factors (cloud free or including the IPA cloud correction) and averaging kernels. A detailed

7 error budget is also provided. Error contributions resulting from each step of the retrieval to

8 the final vertical column error are provided separately, including their random and systematic

9 parts (for details see De Smedt et al., 2014). This allows for an estimation of the total error on

10 the column averages. A quality flag is also provided for each observation. The following

11 criteria are considered for assigning a bad (<0) quality flag:

12 • per orbit: fit residuals larger than three times the averaged fit residual

13 • per day: unsuccessful across-track and zonal reference sector correction (see Sect. 3.2)

14 • per orbit: corrected slant columns lower than the mean corrected column minus three

15   times the column standard deviations

16 • per pixel: effective cloud fractions larger than 0.4

17 • per pixel: snow or ice flag in the cloud product

18 • per pixel: solar zenith angles larger than 70°

19 • per pixel: individual vertical column errors larger than three times the column

4 GOME-2 and OMI H_2CO vertical columns

4.1 Background values and precision

22 Figure **7** presents time series of monthly averaged GOME-2A&B and OMI H_2CO vertical

23 columns in the reference sector (first panel) together with the retrieval residuals, standard

24 deviations and number of observations (second to fourth panels). In the first panel,

25 uncorrected columns are displayed with dotted lines, while background-corrected columns are

26 represented with plain lines. From this figure, it can be concluded that even the uncorrected

27 OMI H_2CO columns are remarkably stable in time (yet across-track and zonal corrections are

28 needed). In the case of GOME-2A retrievals however, the use of radiances as DOAS

29 reference spectra does not completely compensate for a weakening of the signal over the

1 years, although the loss of signal is reduced by a factor 2 compared to the use of solar

2 irradiances, as it was the case in version 12 (De Smedt et al., 2012).

3 Regarding the fit residuals and the standard deviations of the monthly averaged H_2CO

4 columns, the OMI retrievals also show a very good stability in time, the random errors having

5 increased by less than 4% in 10 years, while the GOME-2A random errors have increased at a

6 rate of about 10% per year due to degradation effects. Accordingly, the OMI H_2CO individual

7 pixel precision is about $7x10^{15}$ molec.cm^{-2}, while the GOME-2A precision degraded from

8 $5x10^{15}$ molec.cm^{-2} to $8x10^{15}$ molec.cm^{-2}. The GOME-2B performances are found to be

9 equivalent to those of GOME-2A in its early lifetime; however a degradation rate similar to

10 the one of GOME-2A is expected.

11 As shown in the fourth panel, the number of OMI observations passing our quality criteria has

12 decreased by 40% since the beginning of the mission due to the row anomaly issue. The

13 resulting change of sampling has an impact on the calculated monthly means that should be

14 taken into account in trend analyses (see Sect. 6).

4.2   Continental emission regions

16 Figure 8 presents multi-year maps of H_2CO vertical columns retrieved from GOME-2A and

17 OMI between 2007 and 2013, and their averaged absolute differences over the same period.

18 For these maps (and further below), the quality flags as defined in Sect. 3.4 have been used

19 to filter out invalid satellite observations. We observe consistent H_2CO distributions, with

20 highest columns over tropical regions, India, China, Southeast China and Southeastern US.

21 We also observe noticeable differences, OMI showing more elevated columns at mid-

22 latitudes and over regions with moderate H_2CO concentrations, but lower columns in the

23 Tropics, where the H_2CO columns are highest. To better visualize the regional structures,

24 Figure 9 presents H_2CO vertical columns derived from both sensors over Europe (from April

25 to September) and Asia (from March to November), averaged between 2007 and 2013.

26 Different effects can be identified:

27 (1) The better horizontal resolution of OMI allows for a better identification of strong

28   hotspots over localised H_2CO sources, as for example over cities like Mexico, Pretoria,

29   Hong-Kong/Guangdong, Beijing, Cairo, Tehran and Mumbai. This resolution effect can

30   also be identified along coastal areas (Cape-Town/South Africa, the Algerian Coast, the

15

1   Turkish coasts, Kerala/India or California/US) and along mountain chains (North of

2   India, Pyreneens, Alps).

3   (2) The increase in H_2CO columns between 9h30 and 13h30 –appears to be largest over

4   South Europe, South Australia, Northeastern China or Central Siberia, while an inverse

5   diurnal variation, of equivalent magnitude, is observed over the Equatorial forests of

6   Amazon, Africa and Indonesia. The same effect has been reported for glyoxal columns,

7   another important indicator of NMVOC emissions (Alvarado et al., 2014). The observed

8   diurnal variations will be further discussed in Sect. 5, using ground-based observations.

9   (3) Differences in retrieval sensitivity appear when comparing GOME-2 and OMI. We note

10   that over oceans, poleward of 30°, OMI columns are found to be higher than GOME-2.

11   These differences cannot be explained only by the diurnal variation of the CH_4 oxidation,

12   but they also result from a relative lack of sensitivity of GOME-2 to lower tropospheric

13   H_2CO in comparison to OMI. This is due to the morning overpass time of GOME-2,

14   which leads to larger SZA over mid- and high- latitudes (therefore to lower sensitivity to

15   the lowest atmospheric layers) and to lower H_2CO concentrations (therefore to lower

16   absorption).

17 Table 2Table 2 provides a list of regions where the highest annual H_2CO columns are

18 observed. The annual means are provided with the standard deviations of the monthly

19 averaged columns, as an indication of the amplitude of the seasonal variations. The same

20 regions stand out both in the GOME-2 and OMI observations, with equivalent seasonal

21 variations. However, as shown on the maps, the GOME-2 observations are maximal in the

22 Tropics (Africa and South America), while the OMI observations maximize over megacities

23 like Hong-Kong/Guandong or Delhi. As can be deduced from the seasonal deviations

24 provided in Table 2Table 2, the largest seasonal variations are found in Rondônia/Brazil and

25 Tianjin/China, for both instruments. Interestingly, the OMI H_2CO columns exhibit large

26 seasonal variations along the coasts of India, which are less pronounced in GOME-2

27 observations (Goa, Kerala, Orissa). This could be explained by resolution effects or by

28 diurnal variations in the H_2CO production and loss processes during the monsoon season. In

29 Sect. 6, the complete time series of monthly averaged H_2CO vertical columns in China, India,

30 Africa, South America, North America and Europe are presented.

1   Table 2: GOME-2A and OMI largest annual mean H_2CO columns between 2007 and 2013

2   (10^{15} molec.cm^{-2})

Continent	Country	Province/State	GOME-2A	seas.dev.	OMI	seas.dev.
Africa	Congo		9.37	1.71	7.74	1.27
Africa	Ghana		8.97	2.79	8.47	2.6
Africa	Sierra Leone		10.26	3.76	9.21	3.95
Africa	Togo		8.96	2.77	8.49	2.62
Asia	Bangladesh		9.76	1.48	10.5	2.3
Asia	Cambodia		8.63	3.39	8.74	3.71
Asia	China	Anhui	7.96	2.85	9.21	3.18
Asia	China	Guangdong	8.59	1.44	9.82	1.34
Asia	China	Guangxi	8.6	1.88	9.04	1.63
Asia	China	Hong Kong	9.05	2.25	11.86	3.53
Asia	China	Jiangsu	7.81	3.24	9.39	3.64
Asia	China	Tianjin	7.8	4.75	9.86	3.84
Asia	India	Bihar	9.67	1.44	10.5	2.01
Asia	India	Dadra and Nagar Haveli	7.93	2.32	9.5	3.92
Asia	India	Daman & Diu	8.35	2.5	9.27	4.31
Asia	India	Delhi	10.2	2.85	12.2	2.91
Asia	India	Goa	7.73	3.08	9.41	4.61
Asia	India	Haryana	9.24	2	10.95	2.16
Asia	India	Kerala	7.26	2.76	9.34	4.10
Asia	India	Orissa	9.06	2.38	9.92	3.01
Asia	India	Punjab	9.09	1.97	10.97	2.26
Asia	India	Tripura	8.76	1.68	9.79	2.47
Asia	India	Uttar Pradesh	8.79	1.58	10.2	1.69
Asia	India	West Bengal	9.85	1.61	10.79	2.34
Asia	Singapore		9.14	2.79	8.9	3.62
Asia	Thailand		8.5	3.17	8.79	3.58
South America	Brazil	Mato Grosso	11.19	4.23	8.72	3.82
South America	Brazil	Rondônia	11.04	5.29	8.8	4.71
South America	Brazil	Tocantins	10.55	2.66	8.62	2.57
South America	Bolivia		8.91	2.96	6.19	2.46

3

5 Validation using MAX-DOAS measurements

We validate the observed satellite column variations using ground-based measurements operated by BIRA-IASB at seven stations: Cabauw, Brussels, the Haute-Provence Observatory, Beijing, Xianghe, Bujumbura and Reunion Island. Details of the ground-based measurements, and related publications, are summarized in Table 3~~Table 3~~. In Reunion Island, measurements have been performed with an FTIR instrument (Vigouroux et al., 2009), while in all other stations, multi-axis DOAS (MAX-DOAS) instruments have been used. Although installed at the end of 2013, the Bujumbura instrument could only deliver 6 months of data due to a failure of the UV channel in April 2014.

The MAX-DOAS measurement technique has been developed to retrieve tropospheric trace gas total columns and profiles. The most recent generation of MAX-DOAS instruments allow for measurement of aerosols and a number of tropospheric pollutants, such as NO_2, H_2CO, SO_2, HONO, O_4 and CHOCHO (see e.g. Heckel et al., 2005; Clémer et al., 2010; Irie et al., 2011; Ma et al., 2013, Hendrick et al., 2014; Vlemmix et al., 2014; Wang et al., 2014). H_2CO slant columns have been retrieved from the six MAX-DOAS instruments using consolidated settings published in Pinardi et al. (2013). While the scientific-grade instruments installed in China and in Bujumbura allow for vertical profile retrievals by optimal estimation (Clémer et al., 2010, Hendrick et al., 2014), only vertical columns could be retrieved from the less sensitive instruments operated in the other stations. We therefore use the ground-based total columns to validate the seasonal and diurnal variations in all stations, while a more quantitative validation making use of the profile information is performed in Beijing/Xianghe and Bujumbura.

Table 3: Summary of ground-based measurements available at BIRA-IASB

Station/Country (lat, long)	Instrument	Period	Retrieved quantity	Reference
Cabauw/The Netherlands (52° N, 5° E)	MAX-DOAS	18/06/2009-21/07/2009	VCD	Pinardi et al., 2013
Brussels/Belgium (50.78° N, 4.35° E)	Mini-MAX-DOAS	01/05/2011-23/04/2012	VCD	Gielen et al., 2014
OHP/France (43.94°N, 5.71°E)	MAX-DOAS	26/06/2007-20/03/2013	VCD	Valks et al., 2011
Beijing/China (39.98°N, 116.38°E)	MAX-DOAS	03/07/2008-17/04/2009	VCD + Profile	Vlemmix et al., 2014
Xianghe/China (39.75° N, 116.96° E)	MAX-DOAS	07/03/2010-26/12/2013	VCD + Profile	Vlemmix et al., 2014
Bujumbura/Burundi (3°S, 29°E)	MAX-DOAS	25/11/2013-22/04/2014	VCD + Profile	-
Reunion Island/France (20.9° S, 55.5° E)	FTIR	01/08/2004-25/10/2004 21/05/2007-15/10/2007	VCD	Vigouroux et al., 2009

5.1 Seasonal and diurnal variations

Figure 10 presents the mean diurnal variations of the H_2CO columns, averaged by season over the complete period of measurements, as observed from the ground (in black) and from space (in red). For this figure, measurements in Cabauw and Brussels have been combined, as well as those in Beijing and Xianghe. We therefore consider five validation sites, representative for different emission sources and illumination conditions. The satellite observations are averaged within 100 km around each station, and filtered as described in Sect. 3.4. Although larger than the typical length of air masses sampled by a MAX-DOAS spectrometer, which is less than a few tens of kilometres (Gomez et al., 2014), this radius allows including enough satellite pixels to ensure significant analysis. MAX-DOAS observations are filtered using similar thresholds on total errors (retrieval errors larger than three times the columns) and solar zenith angles (70°). Cloudy observations are excluded using the multiple-scattering cloud filter described in Gielen et al. (2014) since such sky conditions can potentially degrade the quality of the MAX-DOAS retrievals. The error bars shown in Fig.10 include random and systematic error contributions. The random errors are taken as the standard deviations of the daily averaged observations divided by the square root of the number of days considered in the seasonal means. Winter time satellite columns in Europe and China are not shown, because of their reduced quality resulting from a combination of low H_2CO values and lower satellite sensitivity close to the surface. Furthermore, Table Table 4Table 4 provides quantitative differences between the afternoon and morning observations for the five locations, in each season. Both for satellite and ground-based measurements, the correlations between 09h30 and 13h30 columns have been considered to estimate the error on the differences, using a standard uncertainty propagation formulation.

The first conclusion that can be drawn from Fig.10, is the general underestimation of the satellite columns by 0 up to 50% compared to the MAX-DOAS observations especially during the seasons of maximum concentration. In comparison, the agreement is found to be better with tropical background FTIR measurements (Vigouroux et al., 2009). The second conclusion is the qualitative agreement between the satellite and ground-based measurements regarding the H_2CO column variations. The seasonal variations are in a very good agreement, with a maximum in summertime in mid-latitude regions, especially in the South of France and in China. Regarding diurnal variations, the differences between the OMI and GOME-2

19

1   columns should reflect the change in H_2CO between 9h30 and 13h30. However, uncertainties

2   on the satellites H_2CO columns are large (De Smedt et al., 2012), and so are the errors on their

3   differences, as reflected in Table 4Table 4. Nevertheless, the sign of the differences between

4   GOME-2 and OMI agrees well with both MAX-DOAS and FTIR measurements. Early

5   afternoon values are almost always equal to or larger than mid-morning values, except in

6   Bujumbura where morning columns are larger. The amplitude of the diurnal variation inferred

7   from ground-based and satellite data is also in relatively good agreement, as can be seen by

8   comparing the slopes between 09h30 and 13h30, and from Table 4Table 4. This is less true

9   for summertime columns in Brussels/Cabauw, or for spring time columns in OHP and in

10   Beijing/Xianghe, where the differences OMI-GOME-2 are larger than the corresponding

11   MAX-DOAS variations, possibly pointing to an underestimation of the GOME-2 retrievals in

12   those regions/periods.

13   Table 4: Mean diurnal variations of the H_2CO columns as observed with ground-based and

14   satellite instruments. Values are given for 5 regions where BIRA-IASB operates ground-

15   based measurements: Cabauw and Brussels, OHP, Beijing and Xianghe, Bujumbura and

16   Reunion Island. Details of the ground-based measurements are summarized in Table 3Table 3

Station	Instrument	Absolute 13h30-9h30 difference (10^{14}molec.cm^{-2})			
		DJF	MAM	JJA	SON
Cabauw, Brussels	OMI-GOME-2	-	14±24	25±27	21±37
	MAX-DOAS	-	12±25	08±23	20±21
OHP	OMI-GOME-2	-	30±27	34±34	29±34
	MAX-DOAS	00±08	09±10	35±24	18±14
Beijing, Xianghe	OMI-GOME-2	-	34±31	39±67	25±32
	MAX-DOAS	-12±08	-08±18	44±40	18±15
Bujumbura	OMI-GOME-2	-22±26	-28±23	-24±41	-22±40
	MAX-DOAS	-49±28	-50±28	-	-
Reunion Island	OMI-GOME-2	14±22	13±27	16±18	14±30
	FTIR	-	13±20	07±06	06±09

17

5.2 Vertical columns in China and in Burundi

19   Monthly averaged columns retrieved from GOME-2, OMI and MAX-DOAS measurements

20   are shown in Fig.11 and 12, respectively for the stations of Beijing/Xianghe (averaged over

21   2008-2013) and Bujumbura (averaged over 2013-2014). As the instrument in Bujumbura was

22   installed at the end of 2013, we use the more recent H_2CO columns from GOME-2B, but the

GOME-2A columns are shown up to the end of 2013 (light green). The monthly means have been calculated using days in common between respectively GOME-2 and morning MAX-DOAS data (8h-11h), and OMI and afternoon MAX-DOAS data (12h-15h). Again, the satellite observations are averaged within 100 km around each station, and filtered as described in Sect. 3.4. In China, the resulting number of correlative days amounts to 711 for GOME-2 and 807 for OMI. In Burundi, we obtain respectively ~~78~~ 58 and 9~~0~~8 days over the 5 months of measurements. Quantitative comparisons between GOME-2, OMI and MAX-DOAS columns are provided in Table 5.

Three sets of monthly averages are ~~shown~~ used for the satellites, in order to evaluate uncertainties related to the AMF calculation: (1) the vertical columns calculated using the IMAGES *a priori* profile shapes and no cloud correction (plain dots), (2) same but applying the IPA to correct for cloud radiative effects (empty dots), and (3) the vertical columns calculated using as *a priori* the H_2CO vertical profile shapes retrieved from the MAX-DOAS measurements and the IPA cloud correction (diamonds). In Fig.11, the lower panels display scatter plots between monthly averaged observations for the satellite retrievals versions (2) and (3). In Beijing/Xianghe, the correlation coefficients are similarly high between the different AMF versions, and slightly better for OMI than GOME-2 (about 0.8 for GOME-2 and 0.~~85~~9 for OMI). However, the slopes and offests of the regression lines between the satellite and ground-based observations show larger dependency on the AMF calculation settings. We find slopes of respectively 0.~~7~~8, 0.6 and 0.9 for GOME-2 and 0.~~8~~6, 0.~~6~~7, 1.~~1~~ for OMI. In Bujumbura, the number of ground-based measurements is unfortunately not large enough to draw conclusions about the correlations, and we rather provide the mean differences between the satellite and MAX-DOAS columns. The ~~slopes~~ mean differences are found to be respectively ~~0.7, 0.7, and 1.14~~ -2.8,-2.6 and 1.1 x10^{15} molec.cm^{-2} for GOME-2 and ~~0.6, 0.7, and 0.9~~ -3.3,-2.6 and -0.9 x10^{15} molec.cm^{-2} for OMI. Results in China and in Burundi suggest that the cloud correction has little systematic influence, and therefore a limited effect on the monthly averaged columns, as indicated by the mean difference variations between ~~slopes~~ (1) and (2) (~~about~~ less than 10%). On the contrary, the *a priori* vertical profile has a larger systematic effect on the vertical columns, as indicated by the differen~~ce~~t results between ~~slopes~~ (2) and (3). Both for GOME-2 and OMI, switching from modelled to measured profile shapes increase the H_2CO columns by 20 to 50%, bringing the satellites and ground-based observations to a satisfactory agreement within 15%. We note that the OMI columns in Beijing/Xianghe present a positive offset of about 3x10^{15} molec.cm^{-2}.

1 The large effect of the *a priori* profile shape is explained by the vertical sensitivity of the

2 satellite measurements, decreasing strongly in the lowest atmospheric layers, and by the shape

3 of the H_2CO vertical distribution, peaking near the surface. This is illustrated in Fig.13, where

4 the H_2CO profile shapes modelled by IMAGES and those retrieved from the MAX-DOAS

5 measurements, are plotted next to the satellite vertical sensitivity for June 2010 in Xianghe. It

6 must be noted that the retrieved MAX-DOAS profiles also have their own uncertainties

7 (Vlemmix et al., 2014), however using them to re-calculate the satellite AMFs allows to

8 remove from the comparison the error associated to the *a priori* profile shapes (Eskes and

9 Boersma, 2003). Indeed, only the shape of the *a priori* profiles impact the satellite AMFs, not

10 their total columns (Palmer et al., 2001). The satellite averaging kernels (AKs) are much

11 closer in shape to the FTIR AKs than to the MAX-DOAS retrievals, which may explain the

12 better agreement of the columns (Vigouroux et al., 2009).

13 Table 5: Results of the comparisons between GOME2, OMI and MAX-DOAS columns,
14 shown in Figure 11 for Beijing/Xianghe and in Figure 12 for Bujumbura. Three satellite VCs
15 are used: IMAGES a.p. profile/no cloud correction, IMAGES a.p. profile/IPA cloud
16 correction, and MAX-DOAS a.p. profile/IPA cloud correction. Mean differences (satellite-
17 MAX-DOAS) are given in both stations. In Beijing/Xianghe, the slopes and offsets of a linear
18 regression between MAX-DOAS and satellite columns are provided.

	GOME-2			OMI		
	IMAGES ap profiles No cloud correction	IMAGES ap profiles Cloud correction	MAXDOAS ap profiles Cloud correction	IMAGES ap profiles No cloud correction	IMAGES ap profiles Cloud correction	MAXDOAS ap profiles Cloud correction
Beijing/Xianghe						
# common days	711			807		
Mean Difference 10^{15} molec.cm^{-2} (%)	-4.4 (-33%)	-5.4 (-41%)	-1.4 (-11%)	-2.8 (-19%)	-3.4 (-24%)	2.1 (15%)
Correlation coefficient	0.82	0.85	0.84	0.88	0.87	0.88
Slope	0.80	0.64	0.91	0.61	0.62	0.97
Offset 10^{15} molec.cm^{-2}	-1.6	0.6	0.2	3.0	2.3	3.2
Bujumbura						
# common days	58			90		

Mean Difference 10^15 molec.cm^-2 (%)	-2.8 (-29%)	-2.6 (-27%)	1.1 (11%)	-3.3 (-39%)	-2.6 (-31%)	-0.9 (-9%)

The effect of the rather coarse resolution of the global CTM on the modelled profiles (here 2°x2.5°) needs to be further investigated, particularly for anthropogenic sources, as well as possible other effects of vertical transport and chemical processes. For example, a recent analysis of in situ measurements in Beijing (Chen et al. 2014) indicated that primary sources of H_2CO are responsible for as much as about 32% of the total H_2CO source in the area, suggesting a strong underestimation of this direct source in current inventories. In the standard IMAGES simulation using the REASv2 inventory, this primary source contributes to less than 1% of the total H_2CO source during the summer. Adjusting the primary source in the model to match the direct fraction estimated by Chen et al. (2014) results in the IMAGES profile shapes also shown on Fig.13 (IMAGES prim1), found to agree much better with MAX-DOAS profiles. It is not clear whether this large apparent contribution of direct emissions is real or reflects e.g. a fast chemical production from highly reactive VOCs currently not well represented in inventories and models. Whatever the reasons might be for the improved model profiles in comparison with MAX-DOAS data, generalization to other areas would appear premature. It is worth noting that the IMAGES model was found to very well reproduce observed vertical profiles of formaldehyde measured during aircraft campaigns over the United States and over oceans (Stavrakou et al., 2009c). More studies and measurements are required to refine our understanding of factors governing the formaldehyde vertical profiles.

6   Long-term variations

Formaldehyde columns are mainly formed by oxidation of NMVOCs from biogenic, biomass burning and anthropogenic sources. Column inter-annual variabilities are mainly driven by fire events and temperature changes (Millet et al., 2008; Barkley et al., 2009; Stavrakou et al., 2014). However, over industrialised regions, changes in anthropogenic emissions have also been identified as drivers of observed H_2CO column trends (De Smedt et al., 2010; Zhu et al., 2014; Khokhar et al., 2015; Mahajan et al., 2015; Stroud et al., 2015).

The TEMIS time series of morning H_2CO columns, consisting of GOME, SCIAMACHY and GOME-2A & B data, spans over 15 years of observations, while the afternoon time series derived from OMI covers 10 years of observations. Meaningful trend studies are therefore possible. We used a linear model with a seasonal component to fit the monthly averaged columns, separately for the morning and afternoon time series. The error and statistical significance of the inferred trends are also estimated, as described in De Smedt et al. (2010). It is understood that the accuracy of such a trend analysis is limited in the case of H_2CO because, like for the amplitude of the diurnal variation (between 1 and 4 x 10^{15}molec.cm^{-2}), the amplitude of the trends to be detected (about 1-2 x 10^{15}molec.cm^{-2} in 10 years) is one order of magnitude smaller than the H_2CO columns, ~~and~~ their errors and their seasonal variations. However, statistically significant trends are detected in several regions independently with both datasets, which gives confidence in our H_2CO column long-term variation estimates.

Figures 14 to 16 present the time series of monthly averaged H_2CO vertical columns in India, China, ~~India,~~ South America, Africa, ~~South America,~~ North America and Europe. On those figures, the mid-morning time series (in green) combine SCIAMACHY (2003-2011), GOME-2A (2007-2013) and B (from 2013) measurements, while early afternoon columns (in red) are derived from OMI measurements. The good agreement between the different morning observations can be noted (see also De Smedt et al., 2012), as well as the previously described differences and similarities between afternoon and morning time series. In particular, the higher morning columns over tropical forest are also observed in the SCIAMACHY time series. The results of our trend analysis are displayed whenever they have been found statistically significant, i.e. if the absolute value of the calculated trend is larger than twice the associated error. Furthermore, Fig.17 presents a global map of the most significant trends found in the OMI H_2CO columns between November 2004 and August 2014. The analysis has been performed at country level on the global scale, at province or state level in the largest countries, and in a radius of 100 km around the main urban areas.

For these calculations, "sampling-corrected" OMI columns are used. Indeed, as shown in Fig.6, the OMI daily spatial sampling has been reduced over the years because of the growing row anomaly. This has an impact on the H_2CO monthly averaged columns, which tend to decrease in time if this effect is not taken into account. This decrease could be explained by the fact that a large number of central rows (rows 27-44 since January 2009), which have the finest spatial resolution, are affected by the anomaly and need to be filtered out. For this

reason, we have calculated special OMI monthly averages, selecting only the rows that were still valid at the end of 2013. The net effect is a slight decrease of the columns at the beginning of the time series, almost negligible when looking at the absolute values, but significant when considering trends.

In India and China (Fig.14), we observe increasing H_2CO columns. The spatial distribution of the observed increases, and their values, is similar in the SCIAMACHY-GOME-2 and OMI time series. No trend is observed in the largest Chinese cities like Beijing and the Pearl River Delta. However, large positive trends are detected in the surrounding provinces, located in the centre of the country (e.g. Henan and Hunan provinces). This spatial shift of the Chinese trends outside the largest cities was already reported in De Smedt et al. (2010), using GOME and SCIAMACHY observations between 1997 and 2009. This might be related to a larger influence of newer, cleaner technologies in these mega-cities compared to the Chinese heartland (Zhang et al., 2009). In India, we observe positive trends almost everywhere, with an (absolute and relative) amplitude increasing from South to North of the country. Values obtained from morning and afternoon observations are found to be consistent, and similar to the ones reported for the period 1997-2009.

In Eastern US and Western Europe (Figure 16Fig.15), we observe decreasing trends, more clearly detected in the OMI retrievals. The morning H_2CO observations have larger errors and the wintertime observations cannot be used. Negative trends have previously been reported, but with less statistical significance (De Smedt et al., 2010). Here, the correlation between the SCIAMACHY/GOME-2 and the OMI observations is found to be good even in these retrieval-sensitive regions, giving some new confidence in the morning time series over North Europe and North America. The expected negative trends due to emission controls are better captured by the early afternoon observations of OMI, allowing the detection of significant decreases in Germany and France. In South European countries like Spain, negative trends can be detected in both time series, which show remarkable correlation, with for example very low values in spring 2008, that could be related to power plant emission reductions as reported for NO_2 by Curier et al. (2014).

Over the African continent (right panels of Fig.Figure 1516), almost no change is detected, with the exception of Madagascar, and its capital Antananarivo, where a large positive trend is found in the OMI time series. The origin of this trend is not understood for the moment. No similar increase has been reported in satellite NO_2 observations over this region (see for

example Hilboll et al., 2013). In South America (left panels of Figure 15Fig.16), we observe very significant negative trends over the Brazilian state of Rondônia, of -2×10^{14} molec.cm^{-2} yr^{-1}, in both morning and afternoon time series. Such negative trends are also present, with lower amplitudes, in the surrounding Brazilian States covered by the Amazon forest. The largest H_2CO columns worldwide are observed in those regions, with very large variations between the dry and the wet season (see Table 2Table 2). Figure 18 shows the H_2CO columns in Rondônia between 2003 and 2014, the MODIS (on Terra and Aqua satellites) Collection 5 Active Fire Product (ftp://fuoco.geog.umd.edu/modis/C5/cmg, Giglio, 2013), and the yearly deforestation rates reported by the Brazilian INPE (http://www.obt.inpe.br/prodes/index.php), in selected Amazonian States. Deforestation in Rondônia amounted to 23% of its surface area between 1988 and 2013. This is the highest surface ratio among all Brazilian states. The years showing the highest deforestation rates are 1995 and 2004. In Rondônia, a strong decrease of the deforestation rate has been observed between 2005 and 2010, and a slight increase is again observed since 2011. As illustrated by the middle panel of Fig.18, we find high correlation coefficients between the SCIAMACHY/GOME-2 and OMI H_2CO columns and the MODIS fire product, of respectively 0.8 and 0.9 (see also Barkley et al., 2013). We have also compared the H_2CO vertical columns with GISS surface temperature anomalies (Gridded Monthly Maps of Temperature Anomaly Data, http://data.giss.nasa.gov/gistemp/; Hansen et al., 2010), but no correlation was found in this area. Vegetation burning related to deforestation appears to have strongly decreased in Rondônia, while it is not yet the case in the surrounding areas. It should be noted that the strong enhancement of natural fire emissions during very dry years (such as 2005 and 2010), somehow reduce the observed downward trend in the fires and H_2CO columns, and therefore the correlation with the reported deforestation rates.

Besides these direct effects of biomass burning activity changes on the H_2CO columns, more studies are needed in order to assess the impact of deforestation and land use changes, and possibly related meteorological changes, on biogenic NMVOC emissions (Stavrakou et al., 2014). It is worth noting that BIRA-IASB is currently installing a FTIR instrument in Porto Velho, in the Rondônia state. This will bring new information concerning both the diurnal cycle of H_2CO columns and its chemistry, and more generally, on the carbon cycle molecules (CO_2, CH_4, CO and NMVOCs).

7 Conclusions

This paper presents a new version of the BIRA-IASB formaldehyde retrieval algorithm that has been applied to the complete time series of OMI and GOME-2 measurements and delivered for public use on the TEMIS web site. Our focus is the continuity and the consistency of the H_2CO dataset, as well as a good characterisation of the satellite observations. The spectral fits have been improved by means of a better treatment of the interference between O_4, BrO and H_2CO differential structures, resulting in H_2CO columns of higher accuracy and precision. Daily remote radiance spectra are used as DOAS reference, and a destriping procedure is included in the background sector correction, reducing the impact of the OMI row anomaly, but also the GOME-2 across-track variability. Daily morning and afternoon *a priori* profiles are provided by a state-of-the-art version of the IMAGES global CTM.

The GOME-2 and OMI H_2CO datasets agree very well qualitatively, both in terms of long-term variations and seasonal variations. Vertical columns also agree reasonably well although systematic differences are observed depending on the geographical location. The morning H_2CO observations are higher than the afternoon observations over tropical rainforests of Amazon basin, Africa, and Indonesia. The OMI observations are larger than the GOME-2 columns over urban areas (pointing to a horizontal resolution effect) and more generally over all mid-latitude regions (pointing to a combination of actual diurnal variation effects and differences in retrieval sensitivities between morning and afternoon observations).

A detailed validation study has been performed using correlative ground-based MAX-DOAS measurements in Belgium/Netherlands, South of France, North Eastern China, Burundi and FTIR measurements in Reunion Island. We show that the differences observed between the GOME-2 and OMI H_2CO columns are mainly consistent with the diurnal variations observed from the ground, within the error bars of the satellite and ground-based observations. In Beijing/Xianghe and Bujumbura, MAX-DOAS vertical profiles have been used to re-calculate the satellite air mass factors, allowing to eliminate from the comparison the error coming from the *a priori* profiles. By doing so, the satellite and MAX-DOAS columns are found to agree to within 15% or better.

To conclude, while the precision is driven by the signal to noise ratio of the recorded spectra, the accuracy is limited by our current knowledge of the external parameters needed for the retrieval, mainly the a priori profile shapes and their diurnal variation and the cloud and

27

aerosol properties. To fully exploit the potential of satellite data, scientific studies relying on tropospheric H_2CO observations require consistently retrieved long-term time series, provided with well characterised errors and averaging kernels. In the framework of prototype algorithm developments for the future TROPOMI instrument to be flown on the ESA Copernicus Sentinel-5 Precursor mission, we are currently investigating the impact of using global CTM profiles on a finer horizontal resolution. Verification and validation studies are ongoing with the aim to further improve the retrieval algorithms. Furthermore, in the context of the EU QA4ECV project (www.qa4ecv.eu/), a H_2CO Climate Data Record (CDR) using all the satellite instruments based on a jointly optimised European algorithm is currently under development.

8   Acknowledgements

References

Alvarado, L. M. A., Richter, A., Vrekoussis, M., Wittrock, F., Hilboll, A., Schreier, S. F. and Burrows, J. P.: An improved glyoxal retrieval from OMI measurements, Atmos. Meas. Tech., 7(12), 4133–4150, doi:10.5194/amt-7-4133-2014, 2014.

Barkley, M. P., Palmer, P. I., Ganzeveld, L. N., Arneth, A., Hagberg, D., Karl, T., Guenther, A. B., Paulot, F., Wennberg, P. O., Mao, J., Kurosu, T. P., et al.: Can a "state of the art"

chemistry transport model simulate Amazonian tropospheric chemistry?, J. Geophys. Res., 116(D16), D16302, doi:10.1029/2011JD015893, 2011.

Barkley, M. P., De Smedt, I., Van Roozendael, M., Kurosu, T. P., Chance, K. V, Arneth, A., Hagberg, D., Guenther, A. B., Paulot, F., Marais, E. A. and Mao, J.: Top-down isoprene emissions over tropical South America inferred from SCIAMACHY and OMI formaldehyde columns, J. Geophys. Res. Atmos., 118, n/a–n/a, doi:10.1002/jgrd.50552, 2013.

Begoin, M., Richter, A., Weber, M., Kaleschke, L., Tian-Kunze, X., Stohl, A., Theys, N., and Burrows, J. P.: Satellite observations of long range transport of a large BrO plume in the Arctic, Atmos. Chem. Phys., 10, 6515–6526, doi:10.5194/acp-10-6515-2010, 2010.

Boersma, K. F., Eskes, H. J., Dirksen, R. J., van der A, R. J., Veefkind, J. P., Stammes, P., Huijnen, V., Kleipool, Q. L., Sneep, M., Claas, J., Leitão, J., et al.: An improved tropospheric NO_2 column retrieval algorithm for the Ozone Monitoring Instrument, Atmos. Meas. Tech., 4(9), 2011.

Brion, J., et al.: Absorption spectra measurements for the ozone molecule in the 350-830 nm region, J. Atmos. Chem., 30, 291-299, 1998.

Callies, J., Corpaccioli, E., Eisinger, M., Hahne, A., and Lefebvre, A.: GOME-2- Metop's second-generation sensor for operational ozone monitoring, ESA Bull., 102, 28–36, 2000.

Castellanos, P., Boersma, K. F., Torres, O. and de Haan, J. F.: OMI tropospheric NO2 air mass factors over South America: effects of biomass burning aerosols, Atmos. Meas. Tech., 8(9), 3831–3849, doi:10.5194/amt-8-3831-2015, 2015.

Chance, K., Palmer, P. I., Spurr, R. J., Martin, R. V., Kurosu, T. P. and Jacob D. J.: Satellite observations of formaldehyde over North America from GOME, Geophys. Res. Lett., 27, 21, 3461-3464, 2000.

Chance, K. and Kurucz, R. L.: An improved high-resolution solar reference spectrum for earth's atmosphere measurements in the ultraviolet, visible, and near infrared, J. Quant. Spectrosc. Radiat. Transf., 111(9), 1289-1295, 2010.

Chan Miller, C., Gonzalez Abad, G., Wang, H., Liu, X., Kurosu, T., Jacob, D. J., and Chance, K.: Glyoxal retrieval from the Ozone Monitoring Instrument, Atmos. Meas. Tech., 7, 3891-3907, doi:10.5194/amt-7-3891-2014, 2014.

Chen, W. T., Shao, M., Lu, S. H., Wang, M., Zeng, L. M., Yuan, B., and Liu, Y.: Understanding primary and secondary sources of ambient carbonyl compounds in Beijing using the PMF model, Atmos. Chem. Phys., 14, 3047-3062, doi:10.5194/acp-14-3047-2014, 2014.

Choi, S., Wang, Y., Salawitch, R. J., Canty, T., Joiner, J., Zeng, T., Kurosu, T. P., Chance, K., Richter, A., Huey, L. G., Liao, J., Neuman, J. A., Nowak, J. B., Dibb, J. E., Weinheimer, A. J., Diskin, G., Ryerson, T. B., da Silva, A., Curry, J., Kinnison, D., Tilmes, S., and Levelt, P. F.: Analysis of satellite-derived Arctic tropospheric BrO columns in conjunction with aircraft measurements during ARCTAS and ARCPAC, Atmos. Chem. Phys., 12, 1255-1285, doi:10.5194/acp-12-1255-2012, 2012.

Clémer, K., Van Roozendael, M., Fayt, C., Hendrick, F., Hermans, C., Pinardi, G., Spurr, R., Wang, P., and De Mazière, M.: Multiple wavelength retrieval of tropospheric aerosol optical properties from MAX-DOAS measurements in Beijing, Atmos. Meas. Tech., 3, 863-878, doi:10.5194/amt-3-863-2010, 2010.

Curci, G., Palmer, P. I., Kurosu, T. P., Chance, K. and Visconti, G.: Estimating European volatile organic compound emissions using satellite observations of formaldehyde from the Ozone Monitoring Instrument, Atmos. Chem. Phys., 10(23), 11501-11517, 2010.

Curier, L., Kranenburg, R., Segers, a. J. S., Timmermans, R. M. a. and Schaap, M.: Synergistic use of OMI NO2 tropospheric columns and LOTOS–EUROS to evaluate the NOx emission trends across Europe, Remote Sens. Environ., 149(2), 58–69, doi:10.1016/j.rse.2014.03.032, 2014.

Danckaert, T., Fayt, C., Van Roozendael, M., De Smedt, I., Letocart, V., Merlaud, A. And Pinardi, G.: Qdoas Software User Manual, Version 2.108, http://uv-vis.aeronomie.be/software/QDOAS/index.php, 2014.

Daumont, M., Brion, J., Charbonnier, J., and Malicet, J.: Ozone UV spectroscopy, I: Absorption cross-sections at room temperature, J. Atmos. Chem., 15, 145–155, 1992.

De Smedt, I., Müller, J.-F., Stavrakou, T., van der A, R., Eskes, H. and Van Roozendael, M.: Twelve years of global observations of formaldehyde in the troposphere using GOME and SCIAMACHY sensors, Atmos. Chem. Phys., 8(16), 4947-4963, 2008.

De Smedt, I., Stavrakou, T., Müller, J. F., van Der A, R. J. and Van Roozendael, M.: Trend detection in satellite observations of formaldehyde tropospheric columns, Geophys. Res. Lett., 37(18), L18808, doi:10.1029/2010GL044245, 2010.

De Smedt, I.: Long-Term Global Observations of Tropospheric Formaldehyde Retrieved from Spaceborne Nadir UV Sensors, Ph.D. thesis, Universite Libre De Bruxelles, Laboratoire de Chimie Quantique et Photophysique, Faculté de Sciences Appliquées, 2011.

De Smedt, I., Van Roozendael, M., Stavrakou, T., Müller, J.-F., Lerot, C., Theys, N., Valks, P., Hao, N., and van der A, R.: Improved retrieval of global tropospheric formaldehyde columns from GOME-2/MetOp-A addressing noise reduction and instrumental degradation issues, Atmos. Meas. Tech., 5:2933-2949, Special Issue: GOME-2: calibration, algorithms, data products and validation, 2012.

De Smedt, I., Van Roozendael, M., Danckaert, T., Van Gent, J., Theys, N., Lerot, C.: TROPOMI/S5P ATBD of Formaldehyde data product, S5P- BIRA-L2-400F- ATBD, 2014.

Dikty, S. and Richter, A.: GOME-2 on MetOp-A Support for Analysis of GOME-2 In-Orbit Degradation and Impacts on Level 2 Data Products, Final Report, Version 1.2, 14 October 2011.

Dobber, M., Dirksen, R. P. F., Levelt, van den Oord, G. H. J., Voors, R. H. M., et al.: Ozone Monitoring Instrument Calibration, IEEE Transactions on Geoscience and Remote Sensing, 44(5), 1209– 1238, doi:10.1109/TGRS.2006.869987, 2006.

Dobber, M., Q. Kleipool, R. Dirksen, P. Levelt, G. Jaross, S. Taylor, T. Kelly, L. Flynn, G. Leppelmeier, and N. Rozemeijer, Validation of Ozone Monitoring Instrument level 1b data products, J. Geophys. Res., 113, D15S06, doi:10.1029/2007JD008665, 2008.

Eskes, H. and Boersma, K. F.: Averaging kernels for DOAS total-column satellite retrievals, Atmos. Chem. Phys., 1285–1291, 2003.

Fleischmann, O. C., et al. : New ultraviolet absorption cross-sections of BrO at atmospheric temperatures measured by time-windowing Fourier transform spectroscopy, J. Photochem. Photobiol. A, 168, 117–132, 2004.

Fortems-Cheiney, A., Chevallier, F., Pison, I., Bousquet, P., Saunois, M., Szopa, S., Cressot, C., Kurosu, T. P., Chance, K. and Fried, A.: The formaldehyde budget as seen by a global-

scale multi-constraint and multi-species inversion system, Atmos. Chem. Phys. Discuss., 12(3), 6909-6955, doi:10.5194/acpd-12-6909-2012, 2012.

Fu, T.-M., Jacob, D. J., Palmer, P. I., Chance, K. V., Wang, Y. X., Barletta, B., Blake, D. R., Stanton, J. C. and Pilling, M. J.: Space-based formaldehyde measurements as constraints on volatile organic compound emissions in east and south Asia and implications for ozone, J. Geophys. Res., 112(D6), D06312, 2007.

Gielen, C., Van Roozendael, M., Hendrick, F., Pinardi, G., Vlemmix, T., De Bock, V., De Backer, H., Fayt, C., Hermans, C., Gillotay, D., and Wang, P.: A simple and versatile cloud-screening method for MAX-DOAS retrievals, Atmos. Meas. Tech., 7, 3509-3527, doi:10.5194/amt-7-3509-2014, 2014.

Gomez, L., Navarro-Comas, M., Puentedura, O., Gonzalez, Y., Cuevas, E., and Gil-Ojeda, M.: Long-path averaged mixing ratios of O3 and NO2 in the free troposphere from mountain MAX-DOAS, Atmos. Meas. Tech., 7, 3373-3386, doi:10.5194/amt-7-3373-2014, 2014.

González Abad, G., Liu, X., Chance, K., Wang, H., Kurosu, T. P. and Suleiman, R.: Updated Smithsonian Astrophysical Observatory Ozone Monitoring Instrument (SAO OMI) formaldehyde retrieval, Atmos. Meas. Tech., 8(1), 19–32, doi:10.5194/amt-8-19-2015, 2015a.

González Abad, G., Vasilkov, a., Seftor, C., Liu, X. and Chance, K.: Smithsonian Astrophysical Observatory Ozone Mapping and Profiler Suite (SAO OMPS) formaldehyde retrieval, Atmos. Meas. Tech. Discuss., 8(9), 9209–9240, doi:10.5194/amtd-8-9209-2015, 2015b.

Hansen, J., R. Ruedy, M. Sato, and K. Lo: Global surface temperature change, Rev. Geophys., 48, RG4004, doi:10.1029/2010RG000345, 2010

Heckel, A., Richter, A., Tarsu, T., Wittrock, F., Hak, C., Pundt, I., Junkermann, W., and Burrows, J. P.: MAX-DOAS measurements of formaldehyde in the Po-Valley, Atmos. Chem. Phys., 5, 909-918, 2005.

Hendrick, F., Müller, J.-F., Clémer, K., Wang, P., Mazière, M. D., Fayt, C., Gielen, C., Hermans, C., Ma, J., Pinardi, G., Stavrakou, T., Vlemmix, T., and Van Roozendael, M.: Four years of ground-based MAX-DOAS observations of HONO and NO2 in the Beijing area, Atmos. Chem. Phys., 14, 765-781, 2014.

Hewson, W., Bösch, H., Barkley, M. P. and De Smedt, I.: Characterisation of GOME-2 formaldehyde retrieval sensitivity, Atmos. Meas. Tech., 6(2), 371–386, doi:10.5194/amt-6-371-2013, 2013.

Hilboll, A., Richter, A. and Burrows, J. P.: Long-term changes of tropospheric NO2 over megacities derived from multiple satellite instruments, Atmos. Chem. Phys., 13(8), 4145–4169, doi:10.5194/acp-13-4145-2013, 2013.

Ingmann, P., Veihelmann, B., Langen, J., Lamarre, D., Stark, H. and Courrèges-Lacoste, G. B.: Requirements for the GMES Atmosphere Service and ESA's implementation concept: Sentinels-4/-5 and -5p, Remote Sens. Environ., 120(0), 58–69, doi:http://dx.doi.org/10.1016/j.rse.2012.01.023, 2012.

Irie, H., Takashima, H., Kanaya, Y., Boersma, K. F., Gast, L., Wittrock, F., Brunner, D., Zhou, Y., and Van Roozendael, M.: Eight-component retrievals from ground-based MAX-DOAS observations, Atmos. Meas. Tech., 4, 1027-1044, doi:10.5194/amt-4-1027-2011, 2011.

Khokhar, M. F., Khalid, T., Yasmin, N. and De Smedt, I.: Spatio-Temporal Analyses of Formaldehyde over Pakistan by Using SCIAMACHY and GOME-2 Observations, Aerosol Air Qual. Res., 1–14, doi:10.4209/aaqr.2014.12.0339, 2015.

Kleipool, Q. L., Dobber, M. R., de Haan, J. F. and Levelt, P. F.: Earth surface reflectance climatology from 3 years of OMI data, J. Geophys. Res., 113(D18), D18308, doi:10.1029/2008JD010290, 2008.

Kurokawa, J., T. Ohara, T. Morikawa, S. Hanayama, G. Janssens-Maenhout, T. Fukui, K. Kawashima, and H. Akimoto, Emissions of air pollutants and greenhouse gases over Asian regions during 2000–2008: Regional Emission inventory in ASia (REAS) version 2, Atmos. Chem. Phys., 13, 11019-11058, 2013.

Kurosu, T. P., OMHCHO README FILE, http://www.cfa.harvard.edu/_tkurosu/ SatelliteInstruments/ OMI/PGEReleases/READMEs/OMHCHO_README.pdf, 2008.

Leitão, J., Richter, A., Vrekoussis, M., Kokhanovsky, A., Zhang, Q. J., Beekmann, M. and Burrows, J. P.: On the improvement of NO2 satellite retrievals – aerosol impact on the

airmass factors, Atmos. Meas. Tech. Discuss., 2(6), 3221–3264, doi:10.5194/amt-3-475-2010, 2009.

Lerot, C., Stavrakou, T., De Smedt, I., Müller, J.-F. and Van Roozendael, M.: Glyoxal vertical columns from GOME-2 backscattered light measurements and comparisons with a global model, Atmos. Chem. Phys., 10(24), 12059–12072, doi:10.5194/acp-10-12059-2010, 2010.

Levelt, P. F., van den Oord, G. H. ., Dobber, M. R., Malkki, A., Visser, H., de Vries, J., Stammes, P., Lundell, J. O. . and Saari, H.: The ozone monitoring instrument, IEEE Trans. on Geosc. and Rem. Sens., 44(5), 1093–1101, 2006.

Li, C., Joiner, J., Krotkov, N. A. and Dunlap, L.: A new method for global retrievals of HCHO total columns from the Suomi National Polar-orbiting Partnership Ozone Mapping and Profiler Suite, Geophys. Res. Lett., 2515–2522, doi:10.1002/2015GL063204.Received, 2015.

Ma, J. Z., Beirle, S., Jin, J. L., Shaiganfar, R., Yan, P., and Wagner, T.: Tropospheric NO2 vertical column densities over Beijing: results of the first three years of ground-based MAX-DOAS measurements (2008-2011) and satellite validation, Atmos. Chem. Phys., 13, 1547-1567, doi: 10.5194/acp-13-1547-2013, 2013.

Mahajan, A. S., De Smedt, I., Biswas, M. S., Ghude, S., Fadnavis, S., Roy, C. and van Roozendael, M.: Inter-annual variations in satellite observations of nitrogen dioxide and formaldehyde over India, Atmos. Environ., 116, 194–201, doi:10.1016/j.atmosenv.2015.06.004, 2015.

Malicet, C., Daumont, D., Charbonnier, J., Parisse, C., Chakir, A., and Brion, J.: Ozone UV spectroscopy, II: Absorption cross-sections and temperature dependence, J. Atmos. Chem., 21, 263–273, 1995.

Marais, E. A., Jacob, D. J., Kurosu, T. P., Chance, K., Murphy, J. G., Reeves, C., Mills, G., Casadio, S., Millet, D. B., Barkley, M. P., Paulot, F., et al.: Isoprene emissions in Africa inferred from OMI observations of formaldehyde columns, Atmos. Chem. Phys. Discuss., 12(3), 7475-7520, doi:10.5194/acpd-12-7475-2012, 2012.

Martin, R. V, Chance, K. V, Jacob, D. J., Kurosu, T. P., Spurr, R. J. D., Bucsela, E. J., Gleason, J., Palmer, P. I., Bey, I., Fiore, A. M., Li, Q., et al.: An improved retrieval of

tropospheric nitrogen dioxide from GOME, J. Geophys. Res., 107(D20), doi:10.1029/2001JD001027, 2002.

Meller, R., and Moortgat, G. K.: Temperature dependence of the absorption cross section of HCHO between 223 and 323K in the wavelength range 225–375 nm, J. Geophys. Res., 105(D6), 7089–7102, doi:10.1029/1999JD901074, 2000.

Millet, D. B., Jacob, D. J., Boersma, K. F., Fu, T.-M., Kurosu, T. P., Chance, K. V., Heald, C. L. and Guenther, A.: Spatial distribution of isoprene emissions from North America derived from formaldehyde column measurements by the OMI satellite sensor, J. Geophys. Res., 113(D2), 1-18, doi:10.1029/2007JD008950, 2008.

Munro, R., Eisinger, M., Anderson, C., Callies, J., Corpaccioli, E., Lang, R., Lefebvre, A., Livschitz, Y., and Albinana, A. P.: GOME-2 on MetOp, Proc. of The 2006 EUMETSAT Meteorological Satellite Conference, Helsinki, Finland, 2006.

Palmer, P. I., Jacob, D. J., Chance, K. V, Martin, R. V, D, R. J., Kurosu, T. P., Bey, I., Yantosca, R. M. and Fiore, A. M.: Air mass factor formulation for spectroscopic measurements from satellites: Application to formaldehyde retrievals from the Global Ozone Monitoring Experiment, J. Geophys. Res., 106(D13), 14539–14550, doi:10.1029/2000JD900772, 2001.

Palmer, P. I., Abbot, D. S., Fu, T.-M., Jacob, D. J., Chance, K. V., Kurosu, T. P., Guenther, A., Wiedinmyer, C., Stanton, J. C., Pilling, M. J., Pressley, S. N., et al.: Quantifying the seasonal and interannual variability of North American isoprene emissions using satellite observations of the formaldehyde column, J. Geophys. Res., 111(D12), 1-14, doi:10.1029/2005JD006689, 2006.

Pinardi, G., Van Roozendael, M., Abuhassan, N., Adams, C., Cede, A., Clémer, K., Fayt, C., Friess, U., Gil Ojeda, M., Herman, J., Hermans, C., et al.: MAX-DOAS formaldehyde slant column measurements during CINDI: intercomparison and analysis improvement, Atmos. Meas. Tech., 6(1), 167–185, doi:10.5194/amt-6-167-2013, 2013.

Puķīte, J., Kühl, S., Deutschmann, T., Platt, U. and Wagner, T.: Extending differential optical absorption spectroscopy for limb measurements in the UV, Atmos. Meas. Tech., 3(3), 631-653, doi:10.5194/amt-3-631-2010, 2010.

Richter, A., Begoin, M., Hilboll, A. and Burrows, J. P.: An improved NO2 retrieval for the GOME-2 satellite instrument, Atmos. Meas. Tech., 4(6), 213-246, doi:10.5194/amt-4-1147-2011, 2011.

Salawitch, R. J., et al., A new interpretation of total column BrO during Arctic spring, Geophys. Res. Lett., 37, L21805, doi:10.1029/2010GL043798, 2010.

Sander, S. P., J. Abbatt, J. R. Barker, J. B. Burkholder, R. R. Friedl, D.M. Golden, R. E. Huie, C. E. Kolb,M. J. Kurylo, G. K.Moortgat, V. L. Orkin and P. H. Wine : Chemical Kinetics and Photochemical Data for Use in Atmospheric Studies, Evaluation No. 17, JPL Publication 10-6, Jet Propulsion Laboratory, Pasadena, 1320, 2011.

Schultz, M. G., A. Heil, J. J. Hoelzemann, A. Spessa, K. Thonicke, J. G. Goldammer, A. C. Held, J. M. C. Pereira, and M. van het Bolscher, Global wildland fire emissions from 1960 to 2000, Global Biogeochem. Cy., 22, GB2002, doi:10.1029/2007GB003031, 2008.

Stammes, P., Sneep, M., de Haan, J. F., Veefkind, J. P., Wang, P. and Levelt, P. F.: Effective cloud fractions from the Ozone Monitoring Instrument: Theoretical framework and validation, J. Geophys. Res., 113(D16), D16S38, doi:10.1029/2007JD008820, 2008.

Stavrakou, T., Müller, J.-F., De Smedt, I., Van Roozendael, M., van der Werf, G. R., Giglio, L., and Guenther, A.: Global emissions of non-methane hydrocarbons deduced from SCIAMACHY formaldehyde columns through 2003–2006, Atmos. Chem. Phys., 9, 3663-3679, doi:10.5194/acp-9-3663-2009, 2009a.

Stavrakou, T., Müller, J.-F., De Smedt, I., Van Roozendael, M., Kanakidou, M., Vrekoussis, M., Wittrock, F., Richter, A., and Burrows, J. P.: The continental source of glyoxal estimated by the synergistic use of spaceborne measurements and inverse modelling, Atmos. Chem. Phys., 9, 8431-8446, doi:10.5194/acp-9-8431-2009, 2009b.

Stavrakou, T., Müller, J.-F., De Smedt, I., Van Roozendael, M., van der Werf, G., Giglio, L., and Guenther, A.: Evaluating the performance of pyrogenic and biogenic emission inventories against one decade of space-based formaldehyde columns, Atmos. Chem. Phys., 9, 1037-1060, 2009c.

Stavrakou, T., Müller, J.-F., Boersma, K. F., van der A, R. J., Kurokawa, J., Ohara, T., and Zhang, Q.: Key chemical NOx sink uncertainties and how they influence top-down emissions

of nitrogen oxides, Atmos. Chem. Phys., 13, 9057-9082, doi:10.5194/acp-13-9057-2013, 2013.

Stavrakou, T., J.-F. Müller, M. Bauwens, I. De Smedt, M. Van Roozendael, A. Guenther, M. Wild, and X. Xia, Stavrakou, T., Müller, J.-F., Bauwens, M., De Smedt, I., Van Roozendael, M., Guenther, A., Wild, M., and Xia, X.: Isoprene emissions over Asia 1979–2012: impact of climate and land-use changes, Atmos. Chem. Phys., 14, 4587-4605, doi:10.5194/acp-14-4587-2014, 2014.

Stroud, C. a., Zaganescu, C., Chen, J., McLinden, C. a., Zhang, J. and Wang, D.: Toxic volatile organic air pollutants across Canada: multi-year concentration trends, regional air quality modelling and source apportionment, J. Atmos. Chem., doi:10.1007/s10874-015-9319-z [online] Available from: http://link.springer.com/10.1007/s10874-015-9319-z, 2015.

Spurr, R. J. D.: LIDORT and VLIDORT: Linearized pseudo-spherical scalar and vector discrete ordinate radiative transfer models for use in remote sensing retrieval problems, in Light Scattering Reviews, edited by A. Kokhanovsky, pp. 229–271, Berlin, 2008.

Thalman, R. and Volkamer, R.: Temperature dependent absorption cross-sections of O2-O2 collision pairs between 340 and 630 nm and at atmospherically relevant pressure., Phys. Chem. Chem. Phys., 15(37), 15371–81, doi:10.1039/c3cp50968k, 2013.

Theys, N., Van Roozendael, M., Hendrick, F., Yang, X., De Smedt, I., Richter, A., Begoin, M., Errera, Q., Johnston, P. V., Kreher, K. and De Mazière, M.: Global observations of tropospheric BrO columns using GOME-2 satellite data, Atmos. Chem. Phys. Discuss., 10(11), 28635-28685, 2010.

Theys, N., De Smedt, I., van Gent, J., Danckaert, T., Wang, T., Hendrick, F., Stavrakou, T., Bauduin, S., Clarisse, L., Li, C., Krotkov, N., et al.: Sulfur dioxide vertical column DOAS retrievals from the Ozone Monitoring Instrument: Global observations and comparison to ground-based and satellite data, J. Geophys. Res. Atmos., 2014JD022657, doi:10.1002/2014JD022657, 2015.

Valks, P. J. M., G. Pinardi, A. Richter, J. Lambert, N. Hao, D. Loyola, M. Van Roozendael, and S. Emmadi (2011), Operational total and tropospheric NO2 column retrieval for GOME-2, Atmos. Meas. Tech., 4(7), 1491–1514, doi:10.5194/amt-4-1491-2011.

Vandaele, A.C., et al.: High-resolution Fourier transform measurement of the NO2 visible and near-infrared absorption cross-section: Temperature and pressure effects, J. Geophys. Res., 107, D18, 4348, doi:10.1029/2001JD000971, 2002.

van der Werf, G. R., Randerson, J. T., Giglio, L., Collatz, G. J., Mu, Kasibhatla, P. S., Morton, D. C., DeFries, R. S., Jin, Y., and van Leeuwen, T. T.: Global fire emissions and the contribution of deforestation, savanna, forest, agricultural, and peat fires (1997–2009), Atmos. Chem. Phys., 10, 11707–11735, doi:10.5194/acp-10-11707-2010, 2010.

Veefkind, J. P., Aben, I., McMullan, K., Förster, H., de Vries, J., Otter, G., Claas, J., Eskes, H. J., de Haan, J. F., Kleipool, Q., van Weele, M., et al.: TROPOMI on the ESA Sentinel-5 Precursor: A GMES mission for global observations of the atmospheric composition for climate, air quality and ozone layer applications, Remote Sensing of Environment, 120, 70–83, doi:10.1016/j.rse.2011.09.027, 2012.

Vigouroux, C., Hendrick, F., Stavrakou, T., Dils, B., De Smedt, I., Hermans, C., Merlaud, A., Scolas, F., Senten, C., Vanhaelewyn, G., Fally, S., et al.: Ground-based FTIR and MAX-DOAS observations of formaldehyde at Réunion Island and comparisons with satellite and model data, Atmos. Chem. Phys., 9(4), 15891–15957, doi:10.5194/acp-9-9523-2009, 2009.

Vlemmix, T., Hendrick, F., Pinardi, G., Smedt, I. De, Fayt, C., Hermans, C., Piters, A., Wang, P. and Levelt, P.: MAX-DOAS observations of aerosols , formaldehyde and nitrogen dioxide in the Beijing area : comparison of two profile retrieval, Atmos. Meas. Tech., (2), 941–963, doi:10.5194/amt-8-941-2015, 2015.

Vountas, M., Rozanov, V. V., and Burrows, J. P.: Ring effect: impact of rotational Raman scattering on radiative transfer in earth's atmosphere, J. of Quant. Spec. Rad. Trans., 60, 943–961, 1998.

Vrekoussis, M., Wittrock, F., Richter, A. and Burrows, J. P.: GOME-2 observations of oxygenated VOCs: what can we learn from the ratio glyoxal to formaldehyde on a global scale?, Atmos. Chem. Phys., 10(21), 10145-10160, 2010.

Wang, P., Stammes, P., van der A, R., Pinardi, G., and van Roozendael, M.: FRESCO+: an improved O2 A-band cloud retrieval algorithm for tropospheric trace gas retrievals, Atmos. Chem. Phys., 8, 6565-6576, doi:10.5194/acp-8-6565-2008, 2008.

1   Wang, T., Hendrick, F., Wang, P., Tang, G., Clémer, K., Yu, H., Fayt, C., Hermans, C.,

2   Gielen, C., Müller, J.-F., Pinardi, G., Theys, N., Brenot, H., and Van Roozendael, M.:

3   Evaluation of tropospheric SO2 retrieved from MAX-DOAS measurements in Xianghe,

4   China, Atmos. Chem. Phys., 14, 11149-11164, 2014.

5   Wittrock, F., Richter, A., Oetjen, H., Burrows, J. P., Kanakidou, M., Myriokefalitakis, S.,

6   Volkamer, R., Beirle, S., Platt, U., and Wagner, T.: Simultaneous global observations of

7   glyoxal and formaldehyde from space, Geophys. Res. Lett., 33, L16804, 2006.

8   Zhang, Q., Streets, D. G., Carmichael, G. R., He, K. B., Huo, H., Kannari, A., Klimont, Z.,

9   Park, I. S. and Reddy, S.: Asian emissions in 2006 for the NASA INTEX-B mission, Atmos.

10   Chem. Phys., 5131–5153, doi:10.5194/acp-9-5131-2009, 2009.

11   Zhu, L., Jacob, D. J., Mickley, L. J., Marais, E. A., Cohan, D. S., Yoshida, Y., Duncan, B. N.,

12   González Abad, G. and Chance, K. V: Anthropogenic emissions of highly reactive volatile

13   organic compounds in eastern Texas inferred from oversampling of satellite (OMI)

14   measurements of HCHO columns, Environ. Res. Lett., 9(11), 114004, doi:10.1088/1748-

15   9326/9/11/114004, 2014.

16
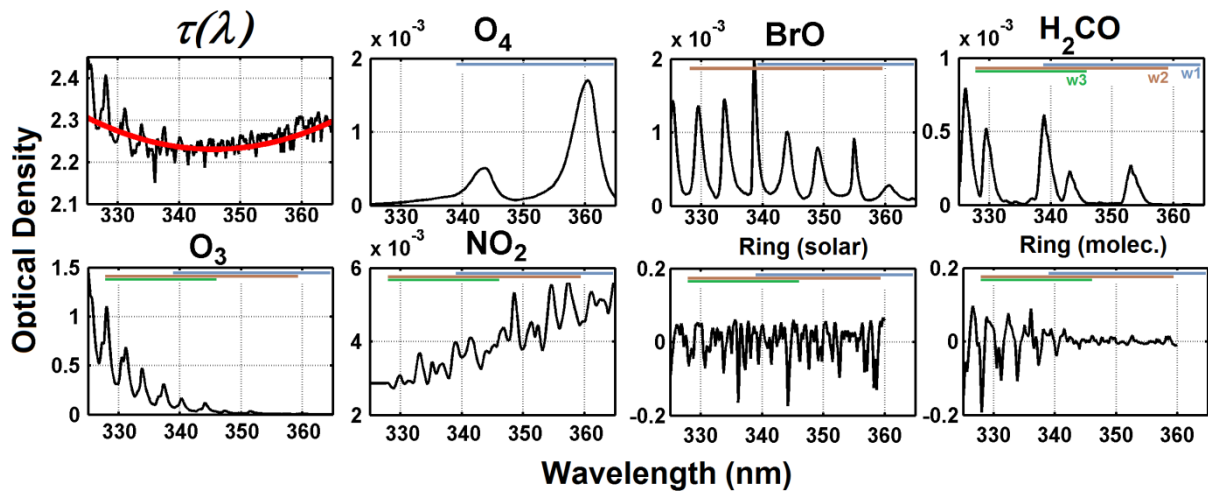
Figure 1: Typical log-ratio of the measured Earth reflectance and fitted low-order polynomial (black and red lines in the first panel), and optical densities of O_2-O_2 (O_4), BrO, H_2CO, O_3, NO_2 and Ring effect (solar lines and molecular) in the near UV. The slant columns have been taken as 0.4×10^{42} $molec^2.cm^{-5}$ for O_4, 10^{14} $molec.cm^{-2}$ for BrO, 10^{16} $molec.cm^{-2}$ for H_2CO, 10^{20} $molec.cm^{-2}$ for O_3 and 1×10^{16} $molec.cm^{-2}$ for NO_2. The different wavelength intervals used in the retrieval are indicated as w1, w2 and w3.
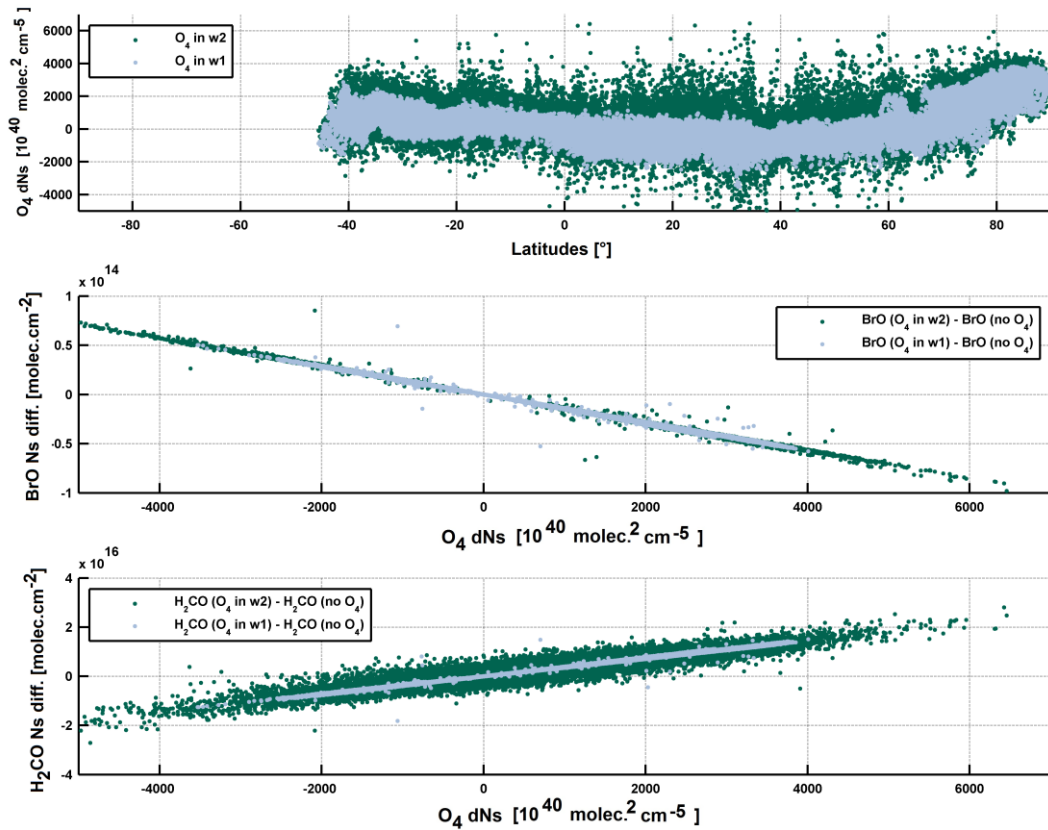
Figure 2: Interdependencies between O_4, BrO and H_2CO slant columns shown for one OMI orbit of 01/07/2005 (UT 0548). The first panel shows the differential O_4 slant columns retrieved in w1 (339-364 nm, light blue) and in w2 (328.5-359 nm, dark green) as a function of the latitude. The second and third panels show the differences obtained in BrO and H_2CO slant columns as a function of the O_4 slant columns, when including or not O_4 in the fits. Differences are shown for two cases: O_4 slant columns retrieved in w1 (light blue) or in w2 (dark green). The limits of the wavelength intervals are indicated in Fig.1.
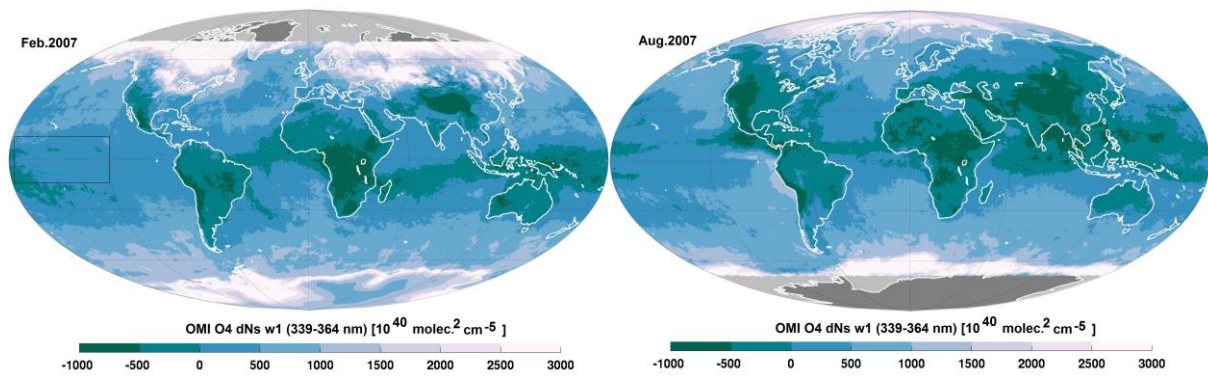
Figure 3: Monthly averaged O_2-O_2 (O_4) differential slant columns retrieved in the interval 339-364 nm. The slant columns are differential since radiance spectra over the Equatorial Pacific region (delimited by the black box) are used as reference spectra.
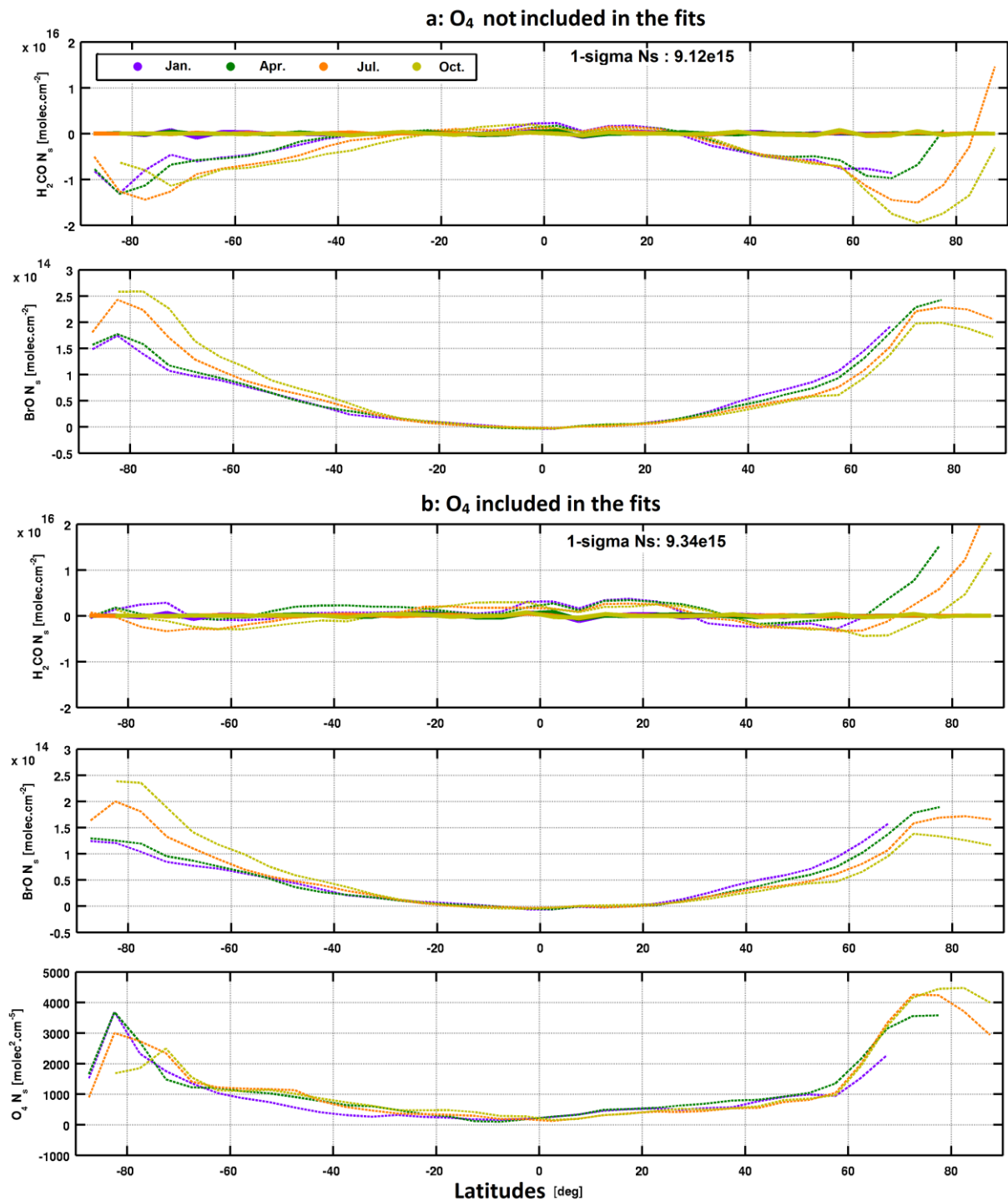
Figure 4: Averaged zonal variation of the H_2CO, BrO and O_4 differential slant columns for 4 months of OMI observations in 2005 (January, April, July, October), over the Pacific Ocean, as a function of the latitude (a) when O_4 is not included in the fit (v12), (b) when O_4 is included and pre-fitted in w1 (v14). Dashed lines show the slant columns before the background normalisation procedure, while the plain lines show the normalized H_2CO slant columns.
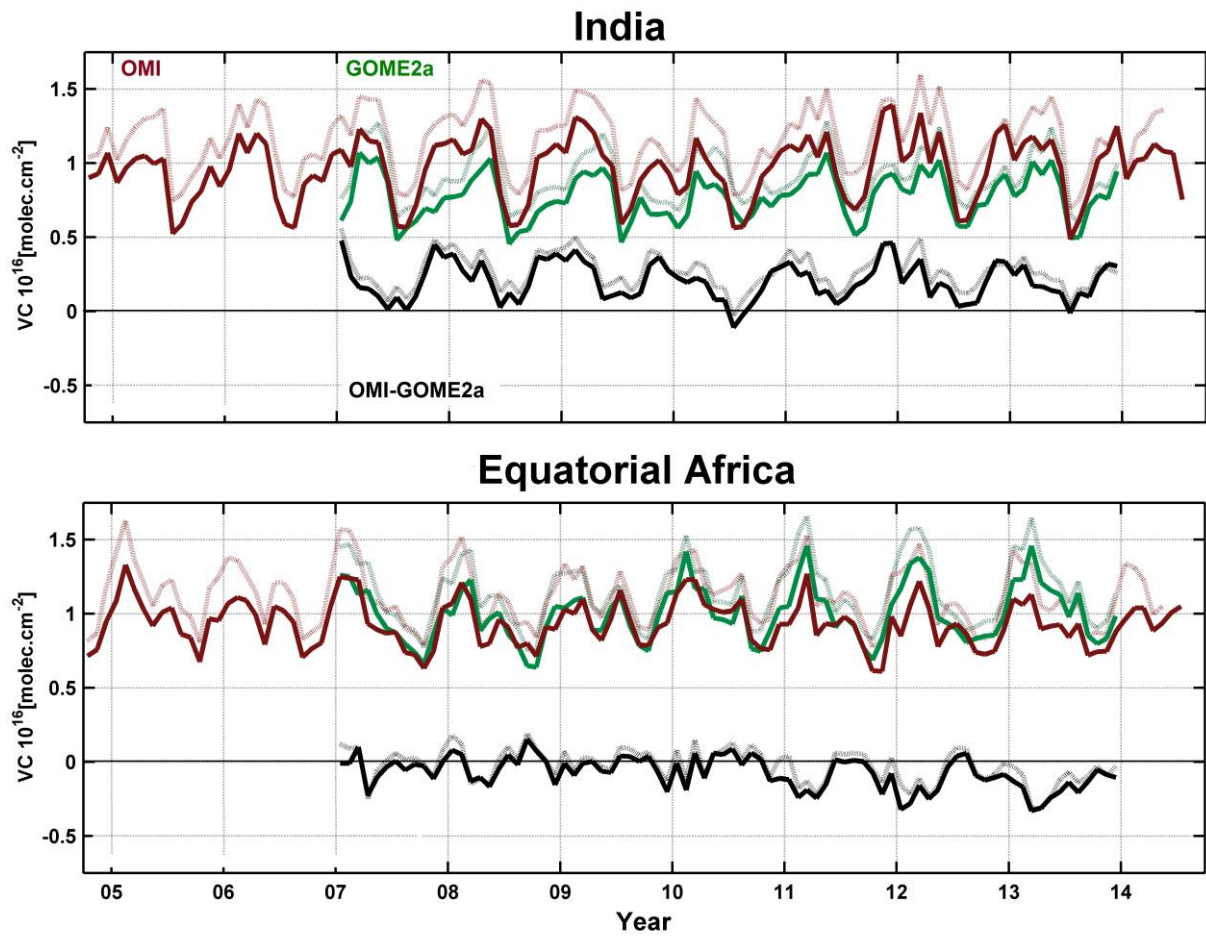
Figure 5: Impact of O_4 on the absolute OMI and GOME-2A H_2CO columns (respectively in red and green) and on their differences (in black). Dashed lines show results when O_4 is not included in the fits, while solid lines show v14 results.
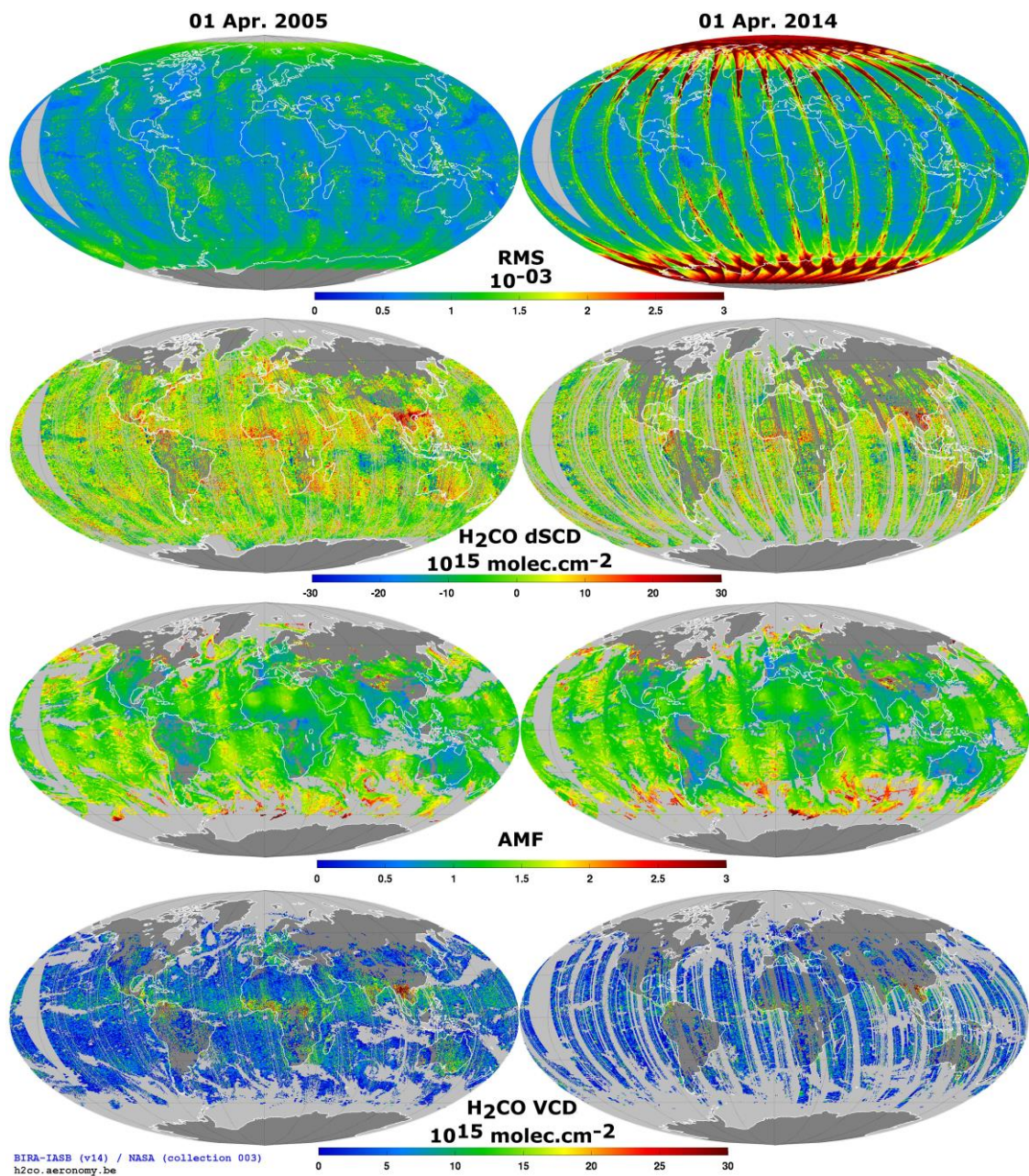
Figure 6: Intermediate retrieval quantities of the H₂CO retrieval algorithm illustrated with OMI on 01 April 2005 (first column), and 01 April 2014 (second column). The first line shows the fit residuals, while lines 2 to 4 show respectively the H₂CO reference sector corrected slant columns, the air mass factors and the vertical columns.
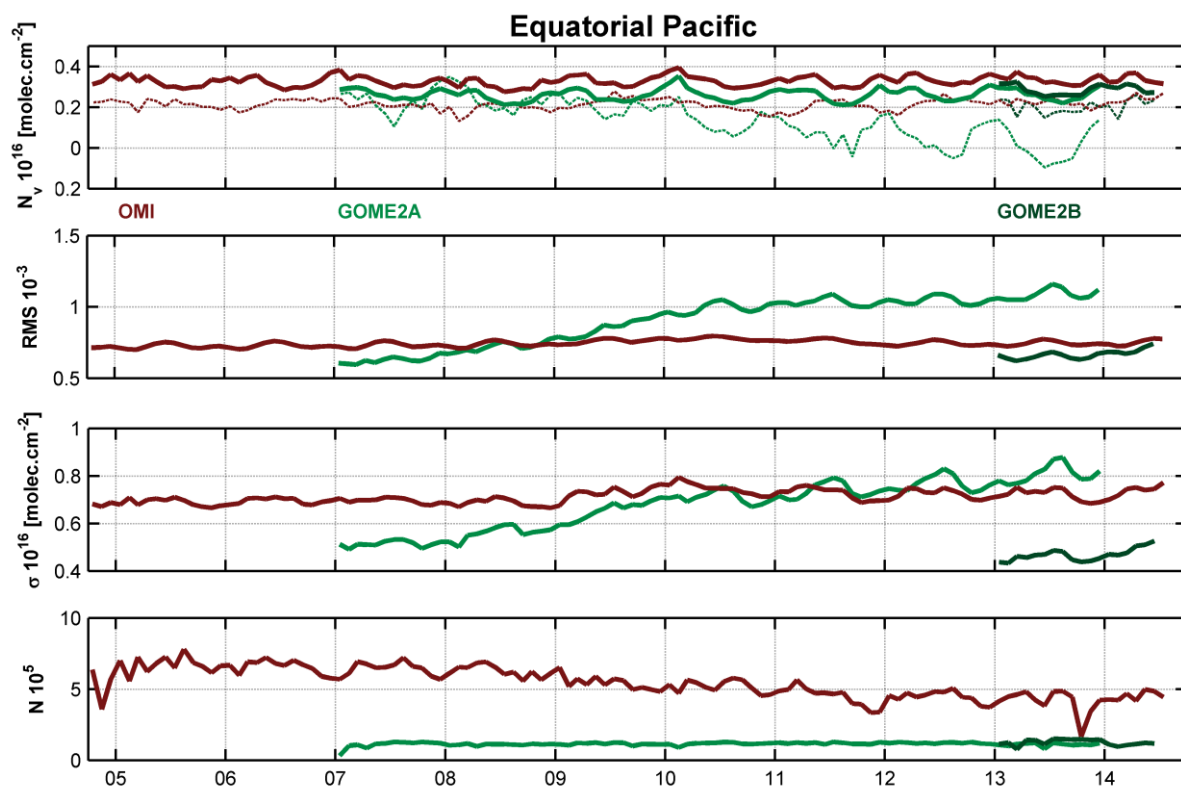
Figure 7: Time series of H₂CO retrieval statistics for OMI and GOME-2 on METOP A and B in the remote equatorial Pacific region ([-15 15]° lat., [180 240]° long.). First panel presents the H₂CO vertical columns, before and after background correction (dotted and plain lines). The second, third and fourth panels present respectively the fit residuals, the column standard deviation and the number of valid observations. See text for details on the DOAS retrieval settings.
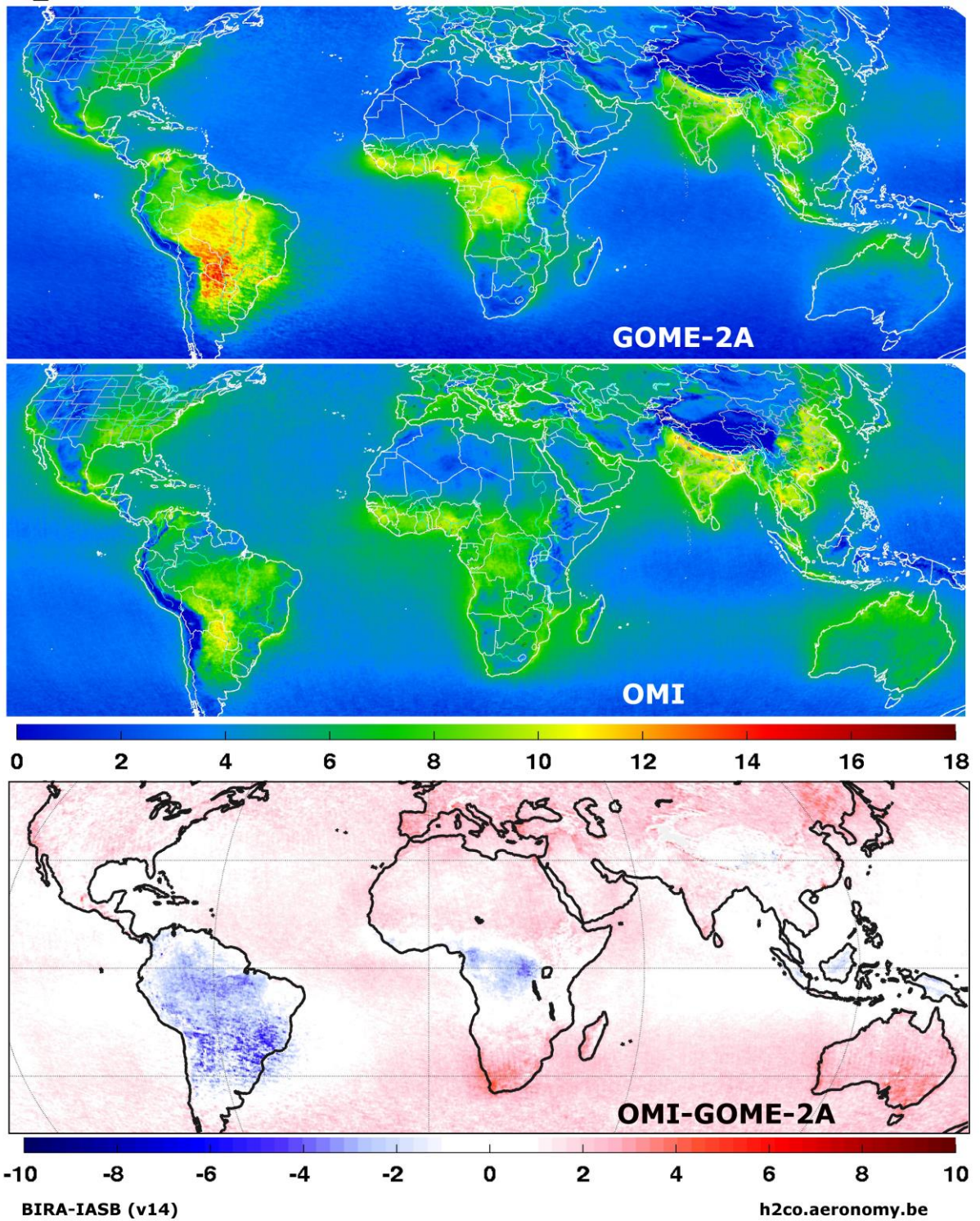
Figure 8: H$_2$CO vertical columns retrieved from GOME-2/MetOp-A (first panel, EUMETSAT level 1 data), OMI/Aura (second panel, NASA level 1 data), and their absolute differences (third panel) between 2007 and 2013.
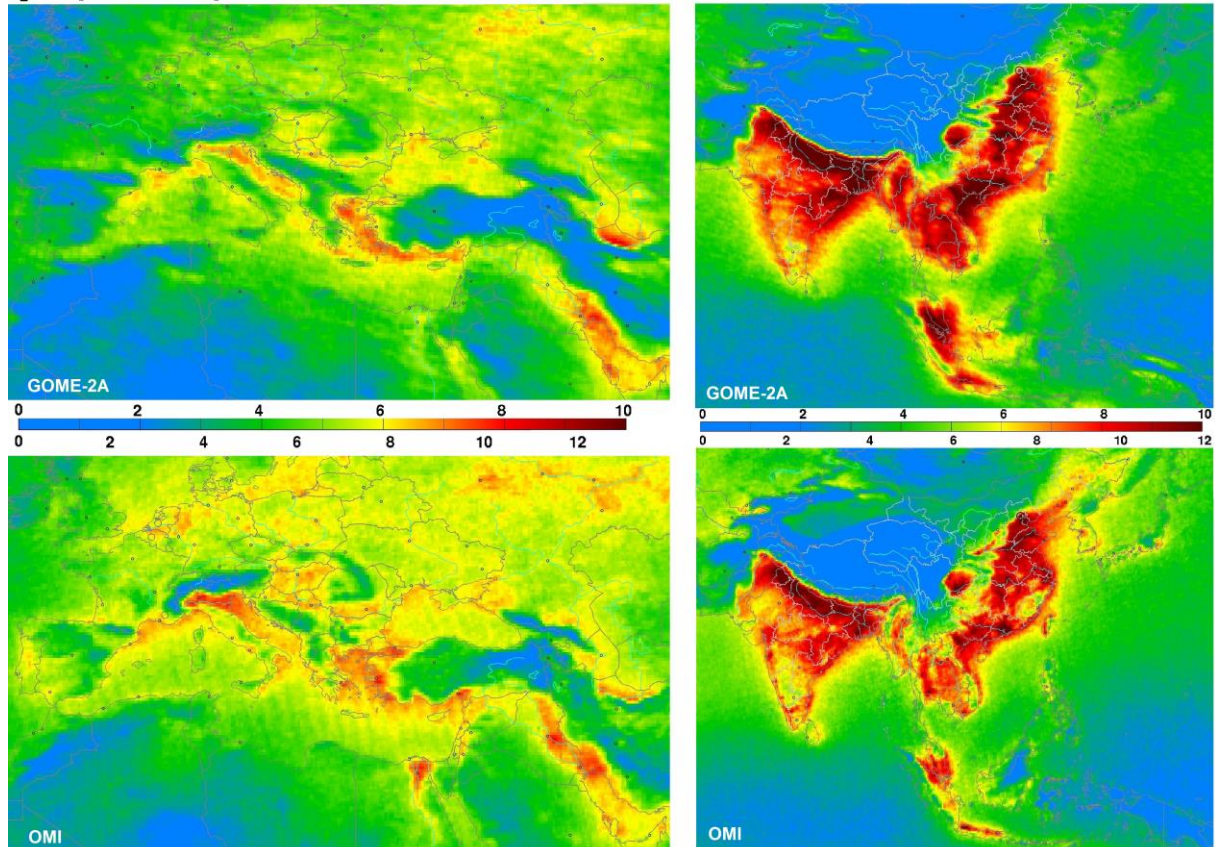
Figure 9: H$_2$CO vertical columns retrieved from GOME-2/MetOp-A (first row) and OMI/Aura (second row) over Europe (from April to September) and Asia (from February to November), between 2007 and 2013. Note that different colour scales have been used for GOME-2 and OMI.
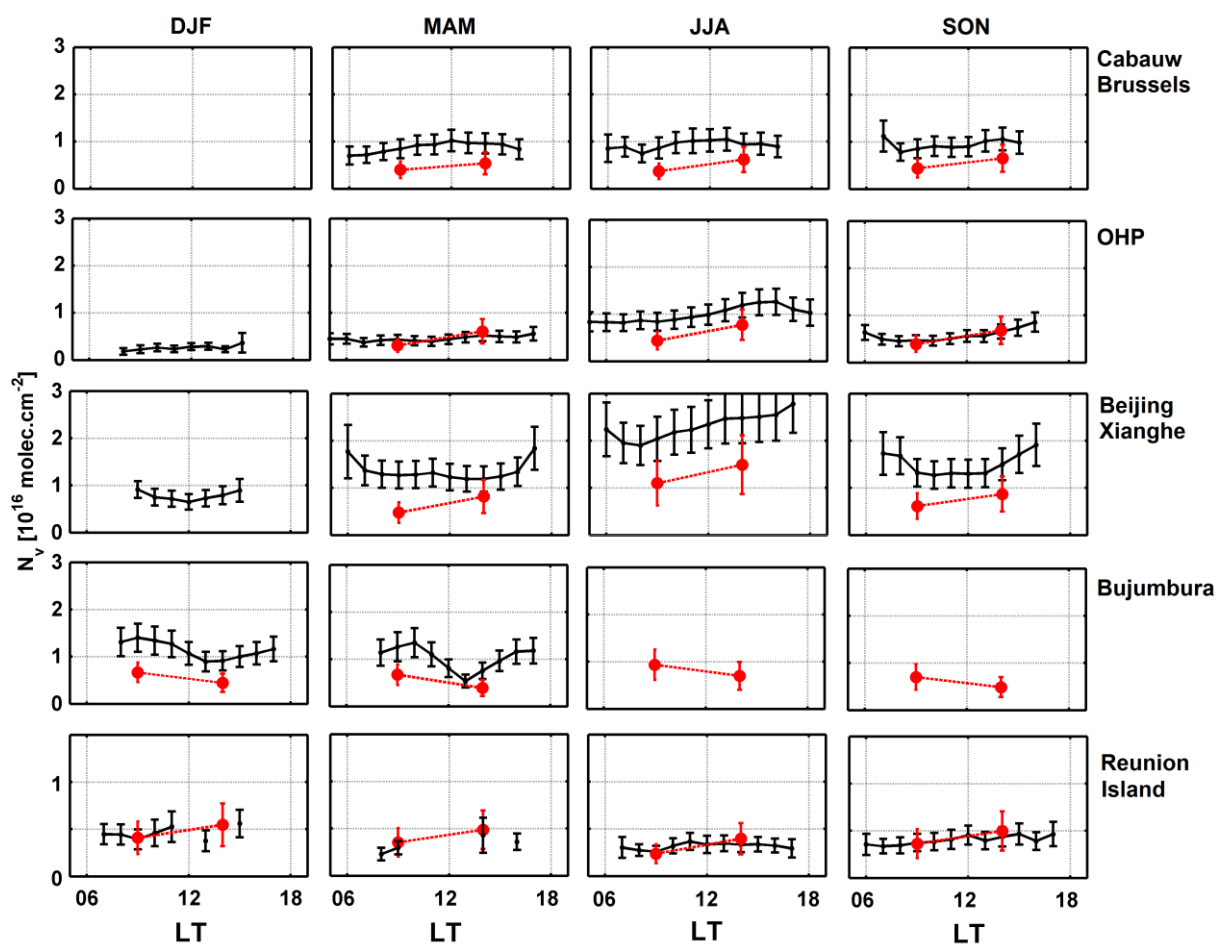
Figure 10: Mean seasonal and diurnal variations of the H$_2$CO columns as observed by MAX-DOAS or FTIR instruments (in black) and by GOME-2 and OMI (in red). Values are shown for 5 regions where BIRA-IASB operates ground-based measurements: Cabauw and Brussels (Northern Europe), OHP (Southern France), Beijing and Xianghe (North Eastern China), Bujumbura (Central Africa) and Reunion Island (Southern Africa). Satellite measurements have been averaged within 100km around each location, and filtered using quality criteria as defined in Sect. 3.4. Details of the ground-based measurements are summarized in Table 3.
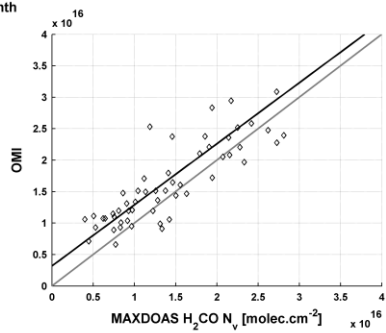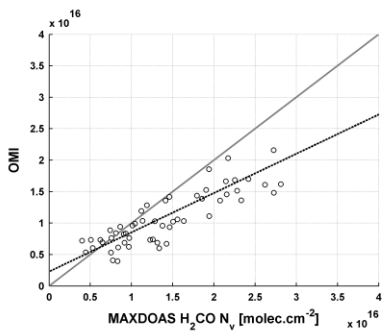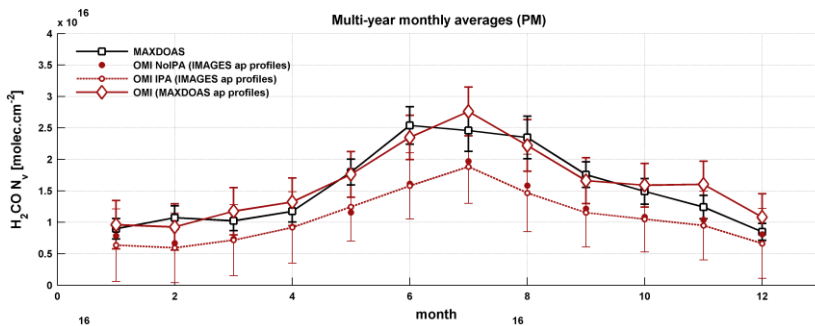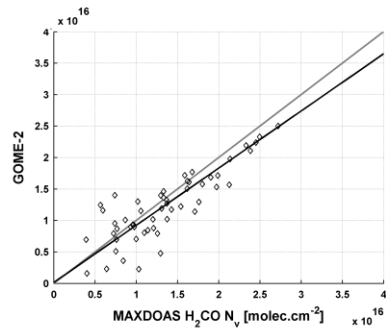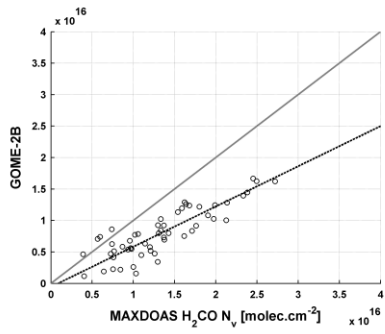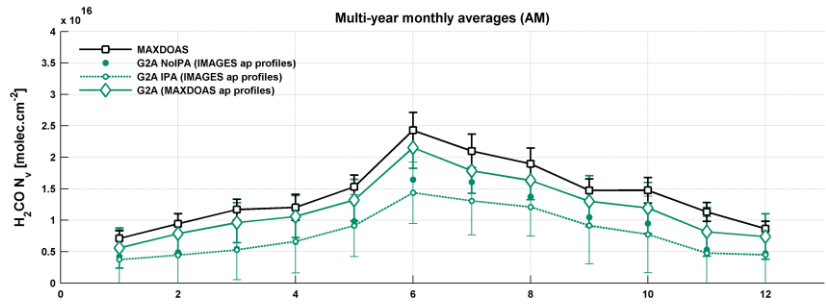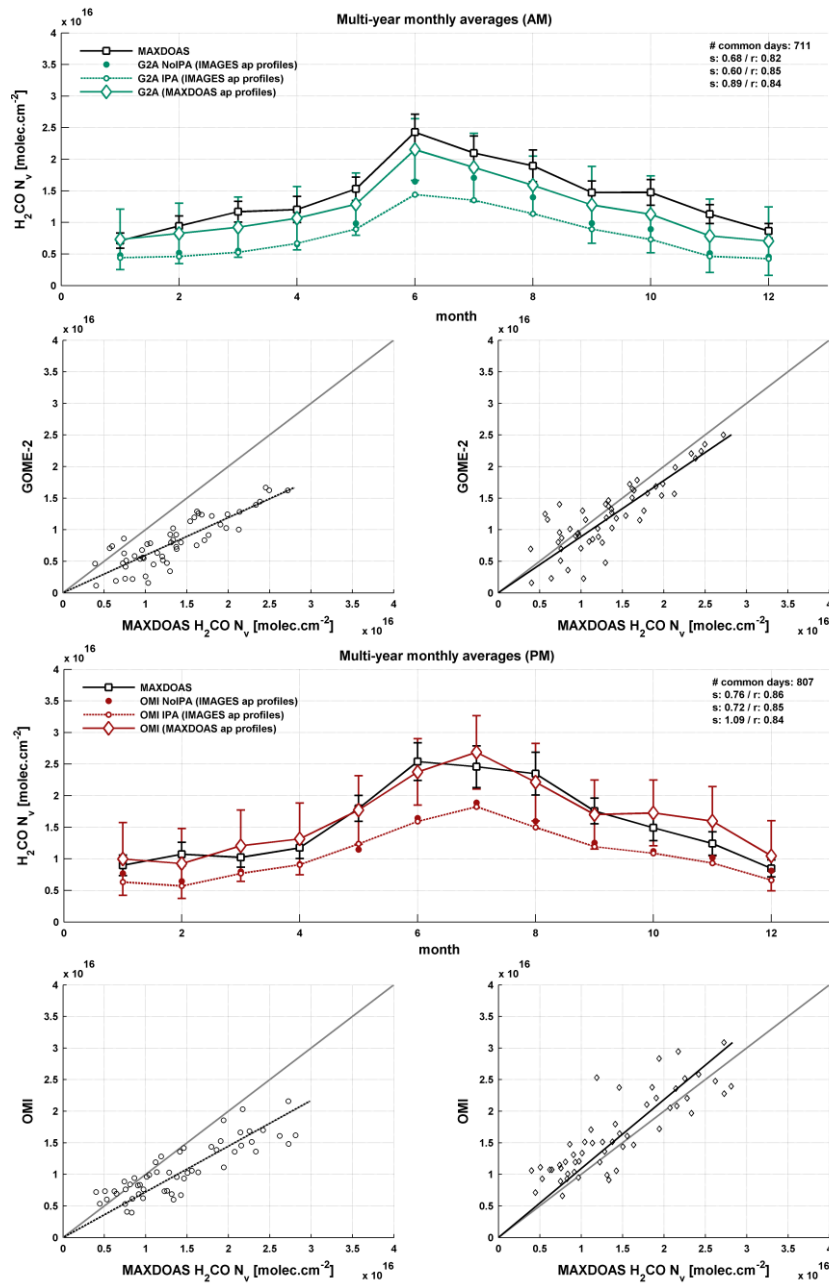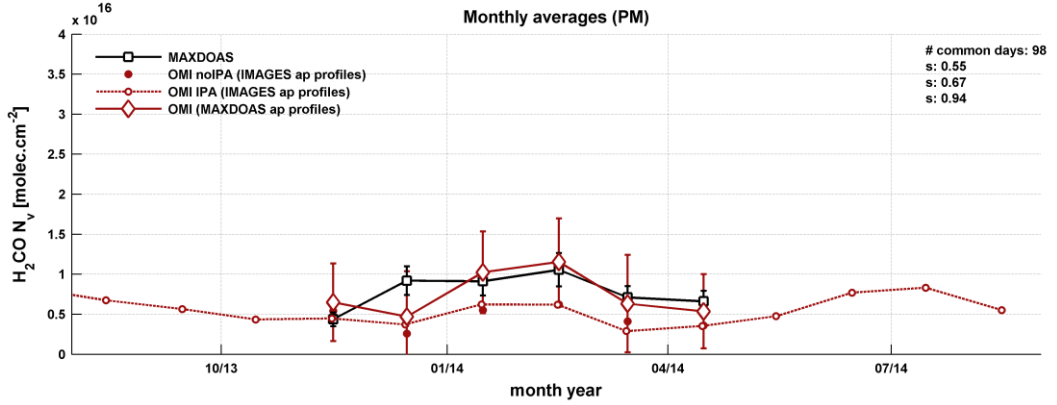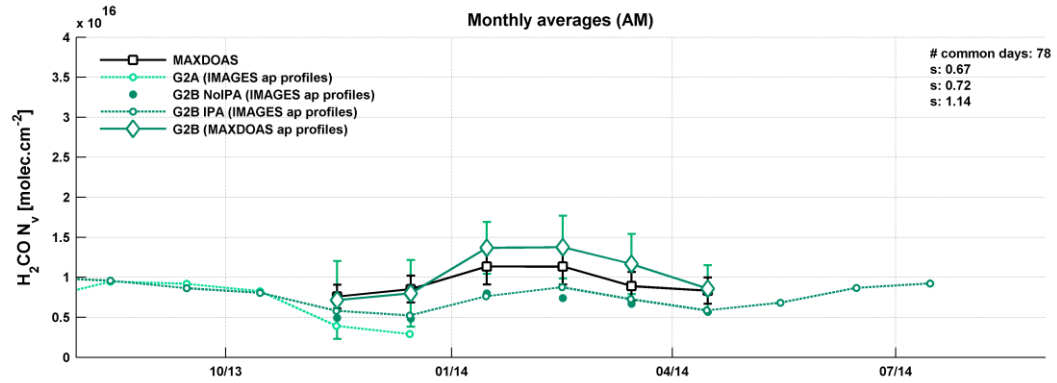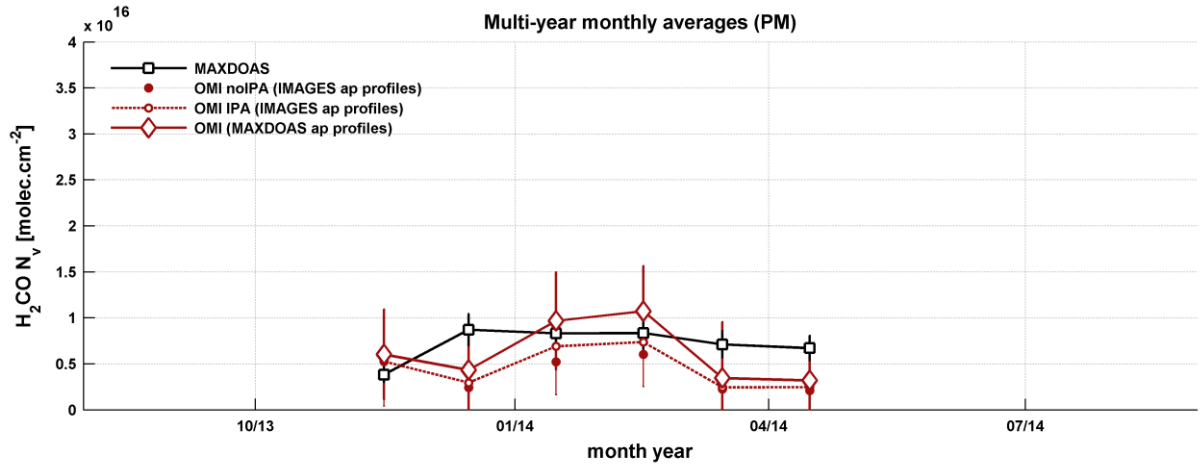
Figure 11: Validation of GOME-2 and OMI retrievals in Beijing and Xianghe, using MAX-DOAS retrievals (represented by black squares). Upper panel: mid-morning observations (GOME-2 and MAX-DOAS averaged over 8-11h). Lower panel: early afternoon observations (OMI and MAX-DOAS averaged over 12-15h). Observations have been averaged per month, over the period 2008-2013, selecting correlative days between GOME-2/OMI and the MAX-DOAS instrument. Satellite measurements have been averaged within 100km around each location, and filtered using quality criteria as defined in Sect. 3.4. Three satellite VCs are presented: IMAGES a.p. profile/no cloud correction, IMAGES a.p. profile/IPA cloud correction, and MAX-DOAS a.p. profile/IPA cloud correction. Correlation plots are shown for the two latter cases, respectively on the left and right panels.

Monthly averages (AM)

Multi-year monthly averages (PM)
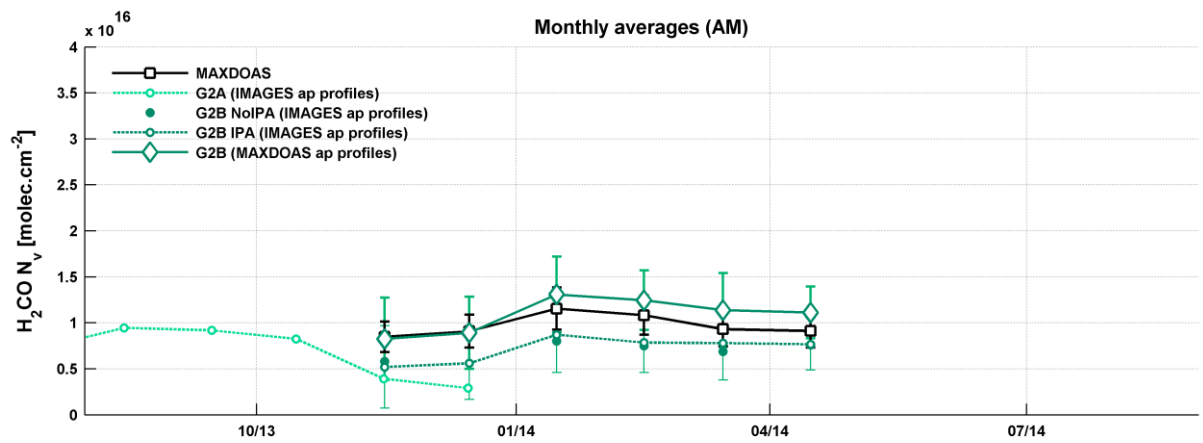
Monthly averages (AM)

Monthly averages (PM)

Figure 12: Validation of GOME-2 and OMI retrievals in Bujumbura, using MAX-DOAS retrievals (represented by black squares). Upper panel: mid-morning observations (GOME-2 A&B and MAX-DOAS averaged over 8-11h). Lower panel: early afternoon observations (OMI and MAX-DOAS averaged over 12-15h). Observations have been averaged per month, over the period 2013-2014, selecting correlative days between GOME-2/OMI and the MAX-DOAS instrument. Satellite measurements have been averaged within 100km around each location, and filtered using quality criteria as defined in Sect. 3.4. Three GOME-2B and OMI VCs are presented: IMAGES a.p. profile/no cloud correction, IMAGES a.p. profile/IPA cloud correction, and MAX-DOAS a.p. profile/IPA cloud correction.
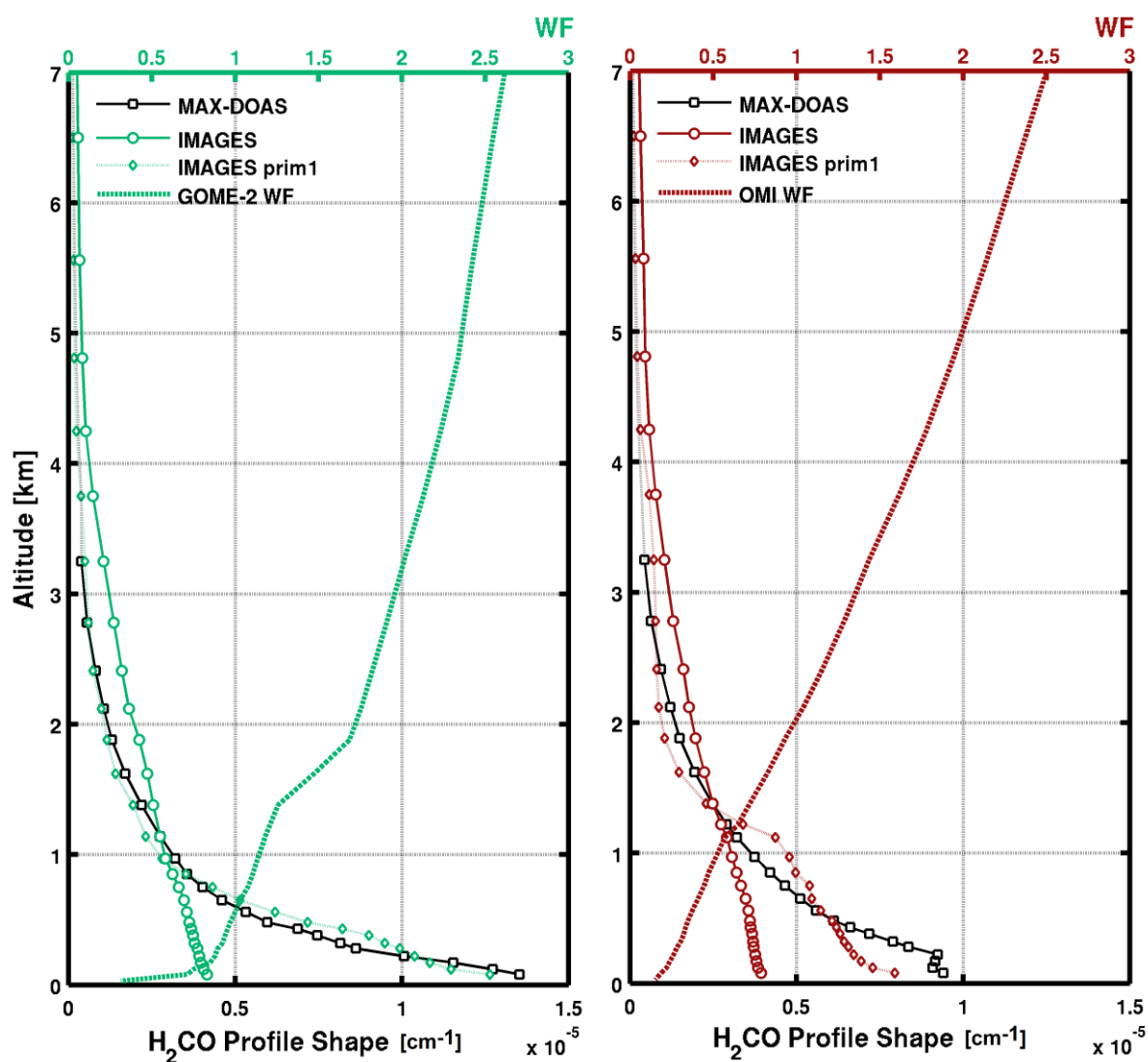
Figure 13: IMAGES CTM and MAX-DOAS retrieved H_2CO profile shapes (concentration profiles divided by their total columns) averaged in June 2010 in Xianghe. IMAGES prim1

includes an additional primary source, as reported by Chen et al. (2014). The corresponding mean satellite scattering weighting function are also displayed.
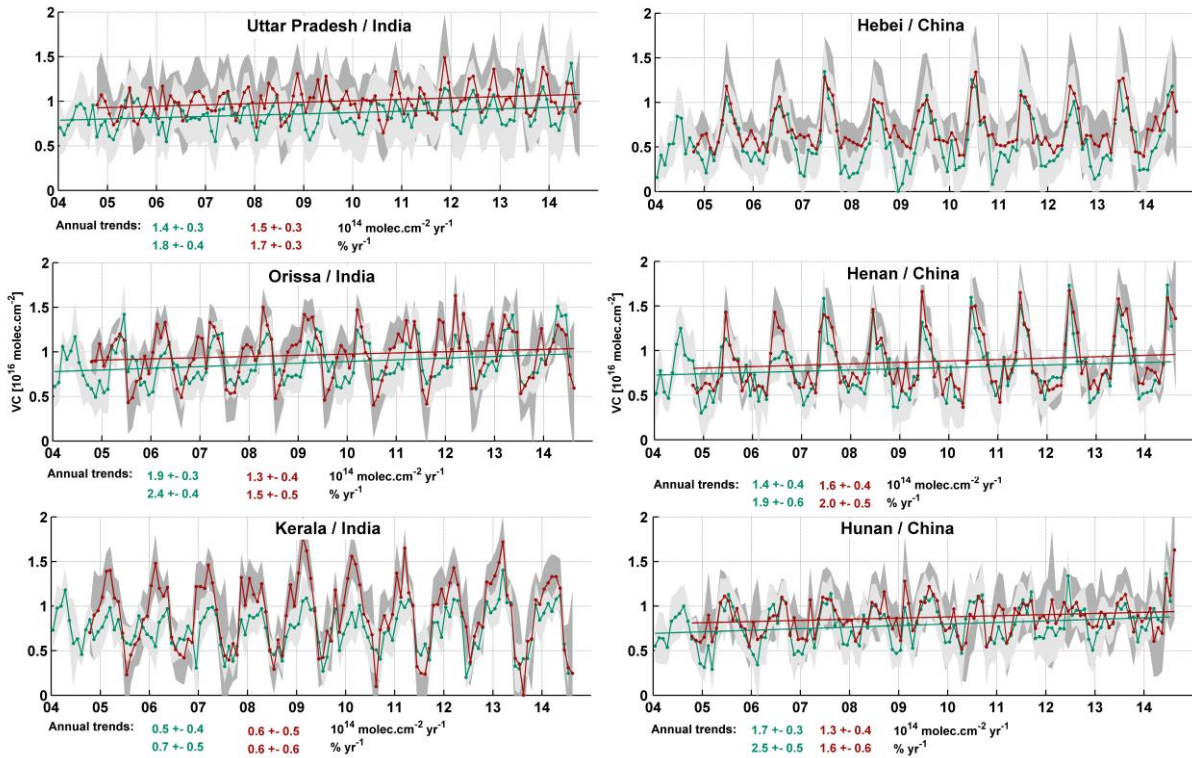

Figure 14: Monthly averaged H_2CO vertical columns as observed from satellite instruments in India and China. Mid-morning columns (in green) consist in SCIAMACHY (2003-2011) and GOME-2A (2007-2013) and B (2013-) measurements, while early afternoon columns (in red) are derived from OMI measurements. If statistically significant, results of the trend analysis are displayed (De Smedt et al., 2010).
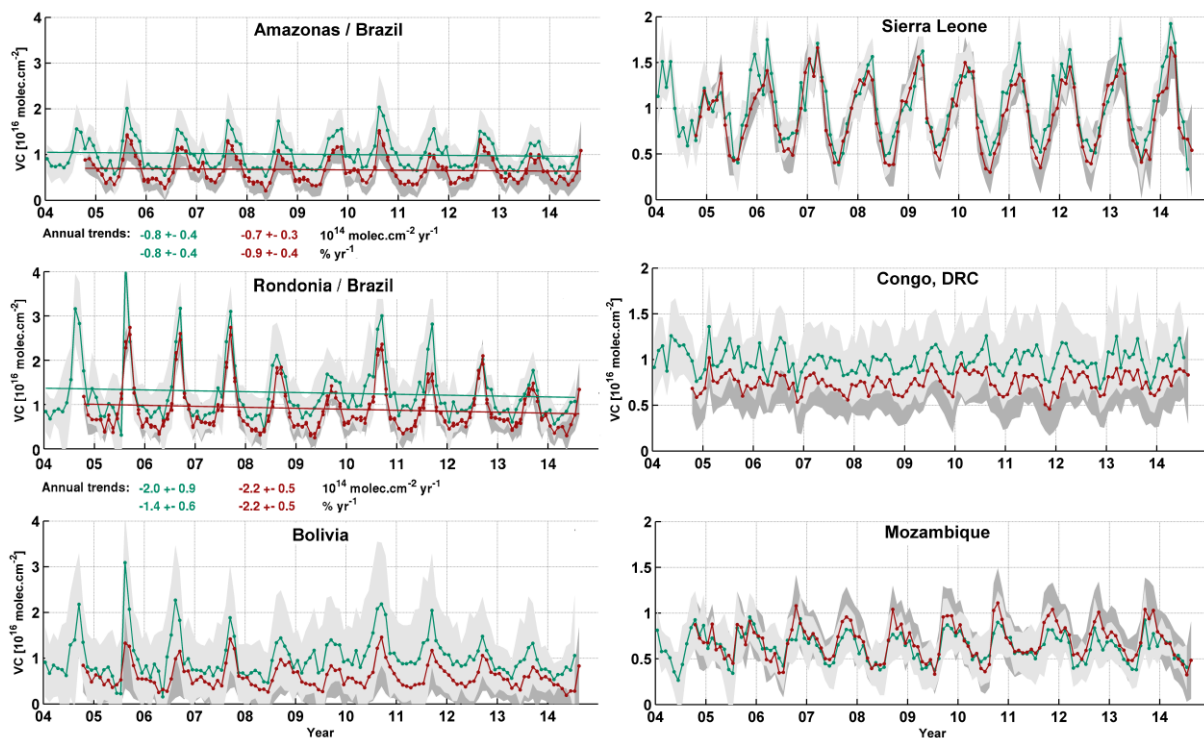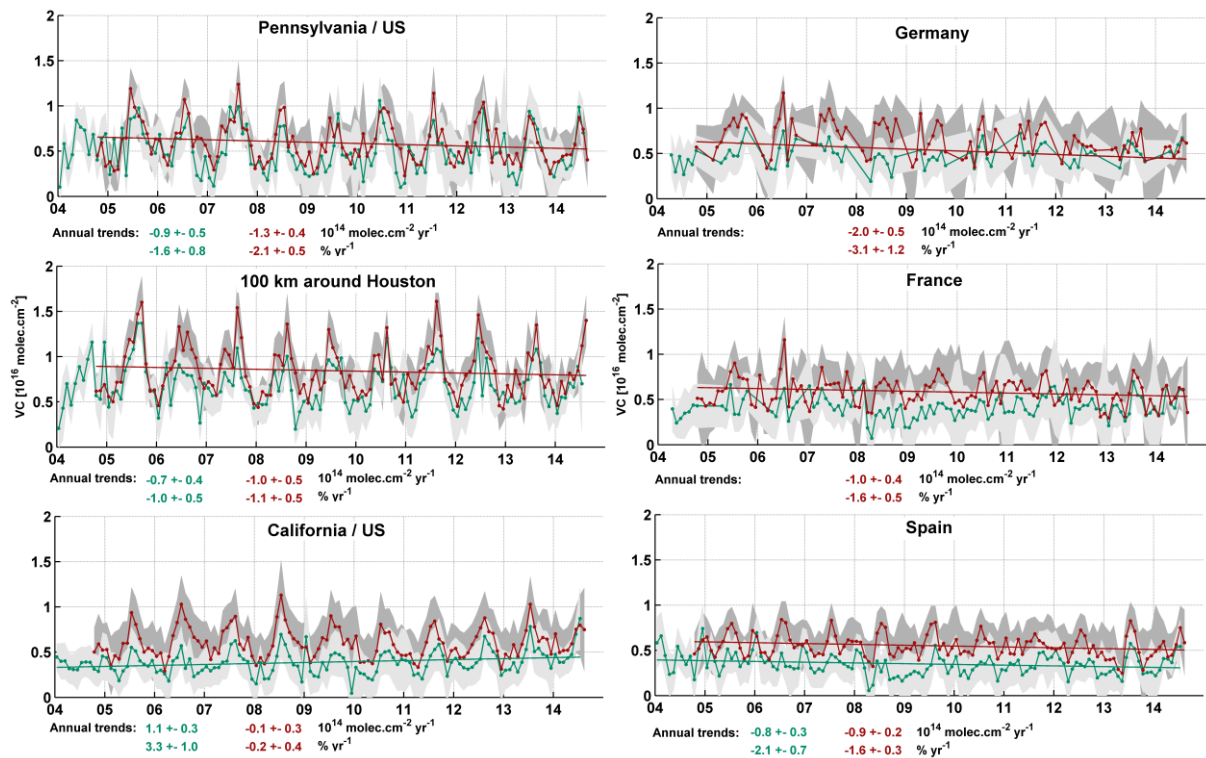
Figure 15: Monthly averaged H_2CO vertical columns as observed from satellite instruments in South America and Africa. Mid-morning columns (in green) consist in SCIAMACHY (2003-2011) and GOME-2A (2007-2013) and B (2013-) measurements, while early afternoon columns (in red) are derived from OMI measurements. If statistically significant, results of the trend analysis are displayed (De Smedt et al., 2010).

Figure 16: Monthly averaged H$_2$CO vertical columns as observed from satellite instruments in US and Europe. Mid-morning columns (in green) consist in SCIAMACHY (2003-2011) and GOME-2A (2007-2013) and B (2013-) measurements, while early afternoon columns (in red) are derived from OMI measurements. If statistically significant, results of the trend analysis are displayed (De Smedt et al., 2010).
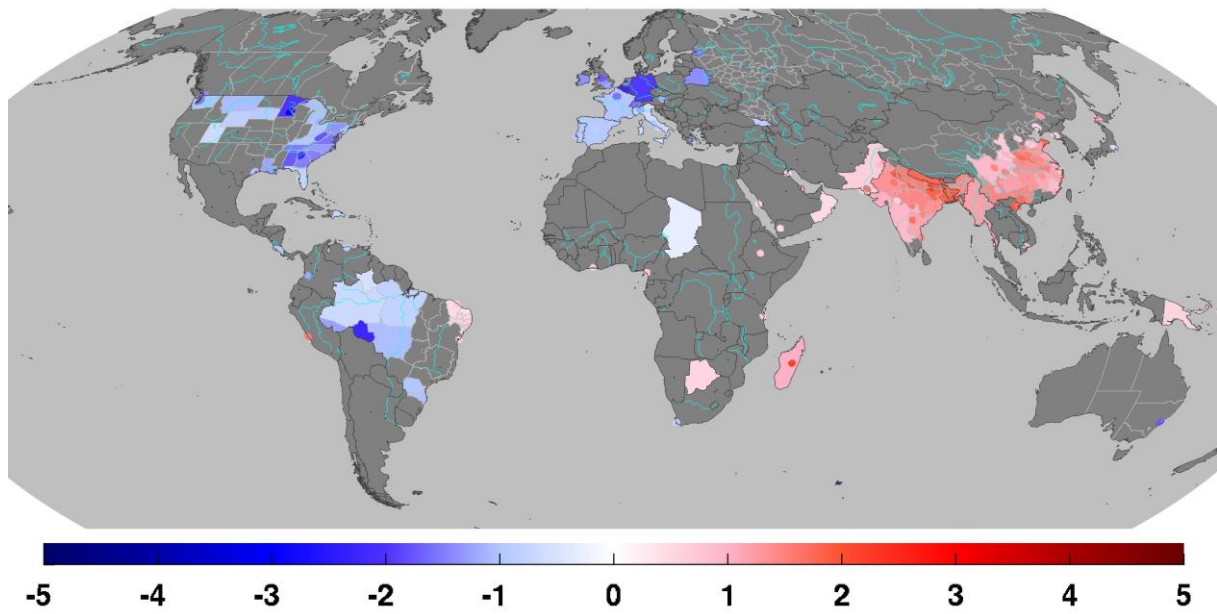
H₂CO Annual Trend [10¹⁴ molec.cm⁻².yr⁻¹]: 2004-2014

Figure 17: Annual absolute trends observed in the OMI H₂CO columns between Nov.2004 and Aug.2014. The change in the OMI spatial sampling over the years has been taken into account in this trend analysis.
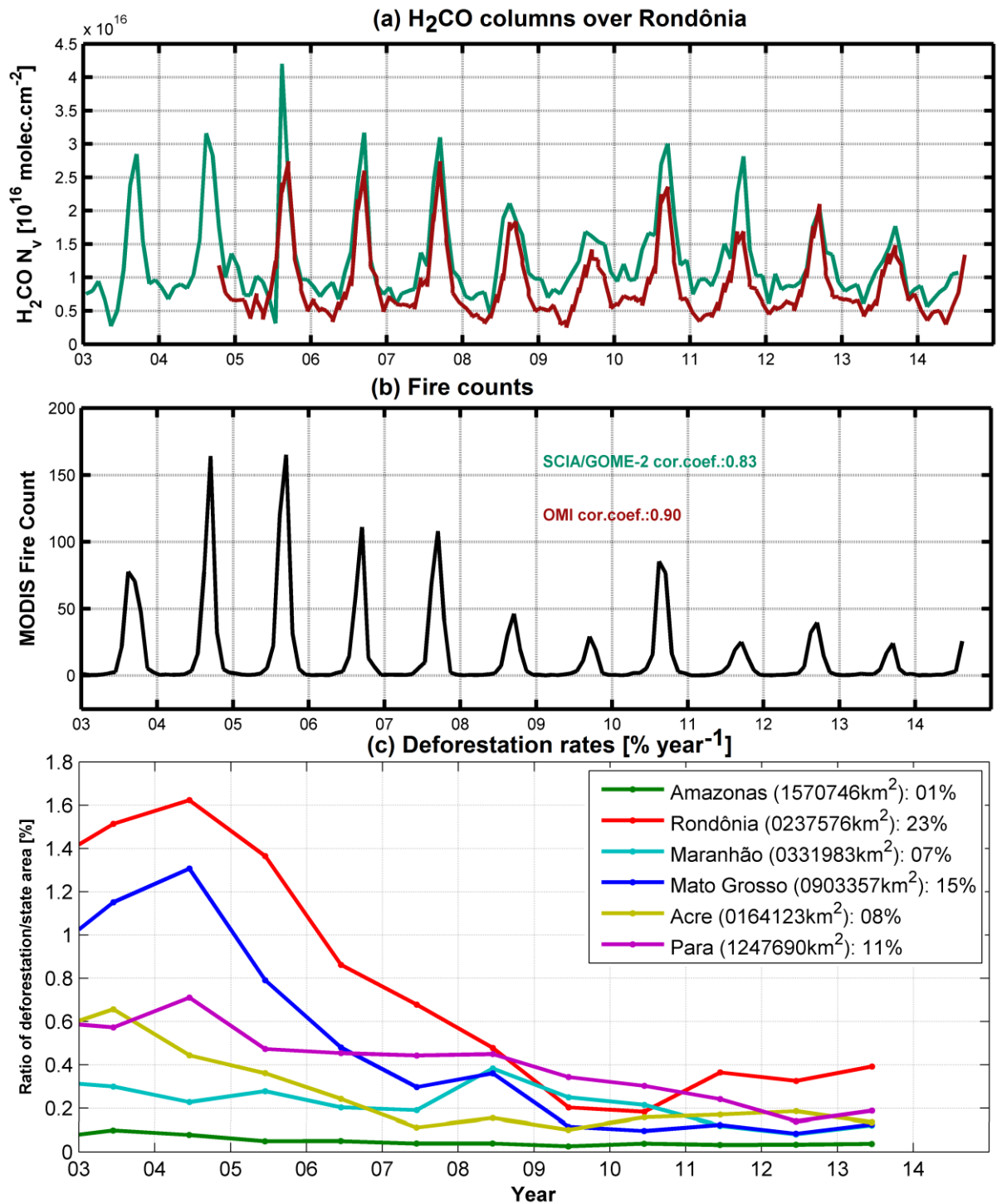
Figure 18: (a) Monthly averaged H$_2$CO vertical columns from SCIAMACHY/GOME2 (in green) and from OMI (in red) (first panel) and (b) MODIS fire count (second panel) over the Rondônia Brazilian State. Inset values are the correlation coefficient between the satellite H$_2$CO columns and the fire counts. (c) Reported yearly deforestation rates in selected Brazilian States, relative to their respective surfaces (third panel, source: Brazil INPE). Inset values are the total surface of the State, and the total rate of deforestation between 1988 and 2013.